
Attributing Emergence in Million-Agent Systems

Ling Tang^{1,2*} Jilin Mei^{1,3*} Qian Chen^{1,4} Qihan Ren^{1,2} Linfeng Zhang²
Quanshi Zhang² Jing Shao¹ Xia Hu¹ Dongrui Liu^{1†}

¹Shanghai Artificial Intelligence Laboratory ²Shanghai Jiao Tong University
³Fudan University ⁴Tongji University

Abstract

Large language models (LLMs) can simulate human-like reasoning and decision-making in individual agents. LLM-powered multi-agent systems (MAS) combine such agents to simulate population-scale social phenomena such as polarization, information cascades, and market panics. Such studies require attributing macro emergence to individual agents, but existing axiomatic methods scale combinatorially in N and have been confined to $N \lesssim 10^3$, while the phenomena they explain occur at $N \geq 10^6$. We address this gap by adapting Aumann–Shapley path-integral attribution to LLM-powered MAS at million-agent scale; the resulting method satisfies all four axioms, runs four to five orders of magnitude faster than sampled Shapley on the same hardware. We use this method to test the scale gap empirically: across 14 days of public Bluesky data (1,671,587 active users), we compute the attribution at both full scale and the visibility-biased $N = 10^2$ convenience sample used by small-scale studies, and the two disagree structurally. At full scale the long tail and middle tier jointly carry the majority; the biased small panel attributes almost everything to a few high-follower accounts. We then prove that under any nonlinear macro indicator the disagreement cannot be reduced by post-hoc rescaling: an Attribution Scaling Bias theorem shows that no global rescaling factor can reconcile small-scale and full-scale attribution. Full-scale attribution is therefore not a methodological choice but a theoretical requirement for any nonlinear macro indicator.

1 Introduction

Large language models (LLMs) can simulate human-like reasoning and decision-making in individual agents [Argyle et al., 2023, Horton, 2023]. Multi-agent systems (MAS) have long been used to study how interactions among autonomous agents produce macro-level emergent phenomena [Wooldridge, 2009]. LLM-powered MAS combine the two, retaining the social realism of LLM agents at the population scale of classical MAS, and have become a common platform for simulating large-scale social phenomena. Recent applications span generative agent societies [Park et al., 2023], macroeconomic activity [Li et al., 2024], financial markets [Yang et al., 2025], and million-agent social platforms [Yang et al., 2024, Piao et al., 2025, Ashery et al., 2025].

These systems reproduce macro emergent phenomena observed in human society, including polarization [Bail et al., 2018], information cascades [Vosoughi et al., 2018, Goel et al., 2016], and market panics [Brunnermeier, 2009]. Scientific use of these reproductions raises two questions about each phenomenon: *which agents drove it?* and *when did it turn?* The macro curve answers neither; both require decomposing the macro indicator into per-agent, per-step contributions.

*Equal contribution. Work done during an internship at Shanghai Artificial Intelligence Laboratory.

†Correspondence to: Dongrui Liu <liudongrui@pjlab.org.cn>

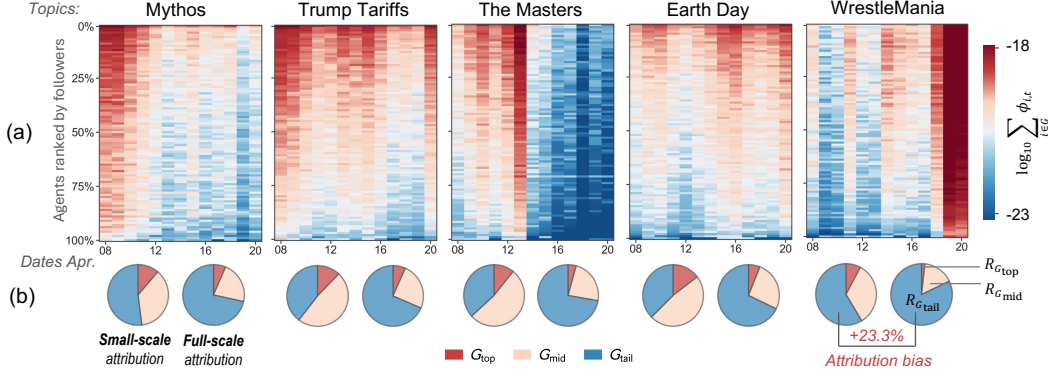


Figure 1: Cross-scale attribution on five Bluesky topics (April 8–21, 2026), $f = f^{\text{heat}}$. **(a)** Per-day attribution at full scale ($N = 1.67 \times 10^6$): rows are agents sorted by follower percentile (high at top, low at bottom), columns are days; cell colour is \log_{10} within-bin attribution mass.

This paper studies emergence attribution in LLM-powered MAS at realistic scale. Existing attribution methods require re-running the simulation over many agent subsets, at cost combinatorial in the number of agents N . Recent adaptations of axiomatic Shapley attribution to LLM-powered MAS [Tang et al., 2026, Lu et al., 2026] remain confined to $N \lesssim 10^3$, while the social phenomena they target, such as online cascades [Vosoughi et al., 2018] and election-period opinion turns [Bond et al., 2012], occur at $N \geq 10^6$. Whether agent-level conclusions drawn at small scale survive at realistic scale is an open question. We give the first systematic answer.

We develop an attribution framework that satisfies the four Aumann–Shapley axioms and scales to millions of agents (Section 4). The framework rests on the Aumann–Shapley path integral [Aumann and Shapley, 1974], reaches $N = 10^6$ in under ten milliseconds, and is four to five orders of magnitude faster than sampled Shapley on the same hardware, over three orders of magnitude (a $1670\times$ jump) beyond the largest agent count reported in prior axiomatic work.

Equipped with this framework, we run a controlled cross-scale study on the complete public Bluesky dataset [Failla and Rossetti, 2024, Seckin et al., 2025] of 1,671,587 active users over April 8–21, 2026 (Section 3). For each topic we attribute the macro indicator both on the full panel and on the visibility-biased convenience sample of $N = 10^2$ that an LLM-powered MAS case study would in practice use. The two answers disagree structurally: at full scale the long tail and middle tier jointly carry the majority of the attribution; under the biased small panel the same axiomatic method places almost all of the mass on a few high-follower accounts (Figure 1, Table 2). A uniform random sample of the same size does not produce the disagreement, so the failure is specific to the biased convenience samples that small- N studies in fact rely on.

Nor can the disagreement be removed by post-processing. Our *Attribution Scaling Bias* theorem (Theorem 1, Section 4) shows that whenever the macro value function is nonlinear, no global rescaling factor can map small-scale attribution onto full-scale attribution; under linearity, exactly one such factor always works. The macro indicators of practical interest, including variance, the Gini coefficient, cascade depth [Goel et al., 2016], and learnable nonlinear value networks, are all nonlinear, so post-hoc correction is generally impossible.

We do not claim that every LLM-powered MAS study must be conducted at million-agent scale. We claim only that any conclusion of the form “*this kind of agent drives this kind of phenomenon*” should rest either on analysis at the phenomenon’s realistic scale or on cross-scale consistency evidence.

2 Related Work

Prior research on LLM-powered MAS has not engaged directly with the scale dependence we report in Section 3. We discuss the three lines of work that bear most directly on agent-level attribution below.

Table 1: Attribution methods compared on two axes: number of axioms satisfied (efficiency, symmetry, dummy, linearity) and the largest agent count reported in published experiments.

Method	Axioms	Reported N
MAST [Cemri et al., 2025]	0/4	< 5
Who&When [Zhang et al., 2025b]	0/4	≤ 5
AgenTracer [Zhang et al., 2025a]	0/4	≤ 5
FAMAS [Ge et al., 2025]	0/4	≤ 5
Leave-one-out [Lu et al., 2026]	3/4	$\sim 10^3$
Banzhaf [Lu et al., 2026]	3/4	$\sim 10^3$
Shapley [Tang et al., 2026]	4/4	$\sim 10^3$
Aumann–Shapley (ours)	4/4	1.67×10^6

Qualitative reproduction of macro emergence in LLM-powered MAS. A first line of work has demonstrated that LLM-powered MAS can reproduce a wide range of social phenomena. Generative agent societies [Park et al., 2023], macroeconomic activity [Li et al., 2024], financial markets [Yang et al., 2025], and large-scale social platforms [Yang et al., 2024, Piao et al., 2025, Gao et al., 2023, Ashery et al., 2025, Tang et al., 2025] have replicated polarization, information cascades, market crashes, and convention formation. Parallel work on collaborative agent pipelines such as AutoGen [Wu et al., 2023], MetaGPT [Hong et al., 2024], ChatDev [Qian et al., 2024], and CAMEL [Li et al., 2023] has reported emergent coordination in task-solving settings, and recent surveys [Mou et al., 2024] have consolidated these directions. We do not add a new emergent phenomenon; we ask who drove a known one, and when.

Axiomatic Shapley-type attribution. A second line has applied cooperative-game attribution to multi-agent settings, building on the Shapley [1953] value and its non-atomic extension by Aumann and Shapley [1974]. The Shapley value has been adapted to multi-agent reinforcement learning for credit assignment [Wang et al., 2020, 2022], to data valuation in machine learning [Ghorbani and Zou, 2019, Jia et al., 2019, Wang and Jia, 2023], and most recently to LLM-powered MAS itself [Tang et al., 2026, Lu et al., 2026]. These methods inherit strong axiomatic guarantees but require evaluating the system on many agent subsets, with cost combinatorial in N ; published experiments accordingly remain at $N \lesssim 10^3$. Leave-one-out and Banzhaf semi-values [Koh and Liang, 2017, Wang and Jia, 2023, Lu et al., 2026] satisfy three of the four axioms (symmetry, dummy, linearity) while losing efficiency, and share the same rerun cost. We retain the same axioms while removing the rerun cost.

Heuristic and prompt-based tracing of MAS failures. A third line has framed agent-level attribution as a labelling problem over execution traces. MAST [Cemri et al., 2025], Who&When [Zhang et al., 2025b], AgenTracer [Zhang et al., 2025a], and FAMAS [Ge et al., 2025] have used trained judges, spectrum-based suspicion scores, or LLM-as-judge prompts to localise faulty agents in failed multi-agent runs. These methods scale to large traces but provide no axiomatic guarantees, and reported agent-level accuracy has remained below 55% on the Who&When benchmark [Zhang et al., 2025b]. We target macro emergence rather than failure, and rely on axioms rather than learned judges.

Table 1 summarises the three lines along the two axes that matter for our use case: how many of the four Aumann–Shapley axioms (efficiency, symmetry, dummy, linearity) the method satisfies, and the largest agent count at which the method has been reported in published work. The Aumann–Shapley attribution we develop in Section 4 retains all four axioms while extending the reported N by over three orders of magnitude (a $1670\times$ jump).

3 Finding: Attribution Flips with Sampling Scale

This section reports the central empirical observation. We use complete public Bluesky data as the empirical testbed: it carries the structural features that LLM-powered MAS studies aim to reproduce (heavy-tailed follower distribution, cross-tier engagement dynamics, real event timing) at the $N \geq 10^6$ scale where the phenomena of interest actually occur. The attribution method itself requires only per-agent features over time and applies unchanged to LLM-powered MAS pipelines; we validate this directly on three LLM-powered MAS scenarios (EconAgent, SocialLLM, MidScale-Social) in Appendix P, where the method matches sampled Shapley wherever sampled Shapley is feasible and extends to scales where it is not.

We attribute the macro indicator at full scale on the Bluesky panel and find that the long tail jointly carries the majority of the attribution (Section 3.1, Figure 1(a)). When we replace the full panel with the small visibility-biased convenience sample that an LLM-powered MAS case study would in practice use, the same axiomatic attribution method concentrates the result on the upper follower tiers (Figure 1(b)). The flip holds across four analytic value functions and across five topics covering technology, politics, sports, society, and entertainment (Section 3.2, Table 2). At realistic scale, full attribution recovers topic-specific temporal structure that the biased small panel collapses to a single shape regardless of topic (Section 3.3).

3.1 Setup

Data. We use the complete public AT-Protocol Jetstream feed of Bluesky from April 8 to April 21, 2026, fourteen days.[‡] After standard filtering (Appendix H) the active panel contains $|[N]| = 1,671,587$ users. We select five topics in distinct domains and report all five in Table 2; the figures focus on the technology-and-subculture topic Mythos because its multi-modal temporal trajectory (no single dominant peak event) makes the per-day cross-tier structure most visible, and the other topics are reported in Appendix H.

Per-agent feature. Each agent i is described by a three-dimensional feature $z_i = (a_i, b_i, c_i)$, where $a_i = \log(1 + \text{followers}_i)$ is reach, $b_i = \log(1 + \text{topic_posts}_i)$ is topic-specific activity, and $c_i = \log(1 + \text{topic_replies_received}_i)$ is topic-specific resonance. For any subset $S \subseteq [N]$ with $|S| = n$, we write $m_d(S) := (1/n) \sum_{i \in S} d_i$ for the per-coordinate mean, $d \in \{a, b, c\}$, and $g_i := a_i + b_i + c_i$ for the per-agent additive composite. The Reach–Activity–Resonance decomposition follows the standard influence schema of Cha et al. [2010] and Riquelme and González-Cantergiani [2016]. Inactive accounts retain a non-zero a_i , so high-follower users without topic engagement can still receive non-zero attribution.

Three-tier follower partition. We rank all $|[N]|$ users by follower count and split them once into three disjoint groups: G_{top} , the top 1% (16,716 users); G_{mid} , the next 9% (150,443 users); and G_{tail} , the remaining 90% (1,504,428 users). Two alternative anchors G_2 and G_3 (top 1% by 7-day post count and 7-day replies received, respectively) are reported in Appendix K; they overlap G_{top} by only 7.7% and 20.1% and serve as independent definitions of “elite”.

Relative attribution share. For any subset $S \subseteq [N]$ and any group G , we report the share of the within- S normalized attribution carried by agents that lie in G :

$$R_G^S := \sum_{i \in S \cap G} \tilde{\phi}_i^S, \quad (1)$$

where $\tilde{\phi}_i^S$ is the normalized Aumann–Shapley attribution of agent $i \in S$ (formally Definition 1 in Section 4, with $\sum_{i \in S} \tilde{\phi}_i^S = 1$ in the cases reported here). Because the three follower tiers partition the panel, $R_{G_{\text{top}}}^S + R_{G_{\text{mid}}}^S + R_{G_{\text{tail}}}^S = 1$ for every subset S . The flip we report below is a structural change in the values of $R_{G_{\text{top}}}^S, R_{G_{\text{mid}}}^S, R_{G_{\text{tail}}}^S$ as S moves from a biased small panel to the full panel.

Four analytic value functions. We instantiate f as four analytic macro indicators, each capturing a different facet of how the panel’s three features aggregate into a scalar:

- $f^{\text{lin}}(z_S) = \frac{1}{n} \sum_{i \in S} (a_i + b_i + c_i)$, the linear additive baseline (Definition 2 satisfied);
- $f^{\text{heat}}(z_S) = \log(1 + m_a(S) m_b(S) m_c(S))$, multiplicative reach \times activity \times resonance with logarithmic saturation, in the spirit of BM25 [Robertson and Walker, 1994];
- $f^{\text{var}}(z_S) = \frac{1}{n} \sum_{i \in S} (g_i - \bar{g}_S)^2$ with $\bar{g}_S = m_a(S) + m_b(S) + m_c(S)$, the population variance of the additive composite;
- $f^{\text{gini}}(z_S) = \frac{1}{2n^2} \sum_{i, j \in S} |g_i - g_j|$, the absolute Gini mean difference [Gini, 1912].

The Aumann–Shapley path-integral attribution $\phi_{i,t}$ used throughout this section is defined formally in Section 4 (Equation 3); the per- f derivations are collected in Appendix F (Equations 11–14). None

[‡]Data ethics, public-data boundaries, de-identification of released artifacts, and misuse-risk considerations are in Appendix I; the firehose endpoint, exact capture window, filtering pipeline, topic-keyword tables, and sampling seeds for end-to-end reproducibility are in Appendix J, and the analysis code will be released as supplementary material.

Table 2: Top-tier relative attribution share $R_{G_{\text{top}}}^S$ across five topics (columns) under three nonlinear value functions (row blocks) and four sampling protocols at $N = 10^2$. Each cell reports $R_{G_{\text{top}}}^S$ in percent followed by $\Delta R_{G_{\text{top}}} := R_{G_{\text{top}}}^S - R_{G_{\text{top}}}^{\text{full}}$ in pp; the FULL row gives $R_{G_{\text{top}}}^{\text{full}}$. Small-panel rows are means over 10 seeds. Full three-tier breakdown, the linear baseline f^{lin} , and standard deviations are in Appendix H (Table 13).

	Mythos (tech)	Trump-Tariffs (politics)	The Masters (sports)	Earth Day (society)	WrestleMania (entertainment)
<i>f^{heat} multiplicative-saturating heat</i>					
BIAS _v	11.3 (+7.6)	12.1 (+5.6)	10.8 (+6.4)	14.7 (+9.3)	7.8 (+6.0)
BIAS _{xf}	5.8 (+2.1)	10.5 (+3.9)	6.1 (+1.7)	9.3 (+3.9)	2.2 (+0.4)
BIAS _{top}	5.7 (+2.1)	9.9 (+3.3)	7.4 (+3.0)	7.9 (+2.5)	2.2 (+0.4)
RAND	0.8 (-2.9)	2.4 (-4.2)	7.4 (+3.0)	0.8 (-4.6)	0.8 (-1.0)
FULL	3.7	6.5	4.4	5.4	1.8
<i>f^{var} population variance</i>					
BIAS _v	78.3 (+68.6)	70.7 (+61.0)	79.3 (+69.7)	74.9 (+65.2)	79.5 (+69.9)
BIAS _{xf}	25.2 (+15.6)	45.8 (+36.0)	28.1 (+18.5)	32.4 (+22.7)	10.1 (+0.5)
BIAS _{top}	23.3 (+13.7)	40.8 (+30.9)	34.4 (+24.8)	28.5 (+18.9)	9.8 (+0.2)
RAND	7.4 (-2.3)	7.4 (-2.4)	7.6 (-2.0)	7.3 (-2.4)	7.4 (-2.2)
FULL	9.7	9.8	9.7	9.7	9.6
<i>f^{gini} absolute Gini mean difference</i>					
BIAS _v	63.5 (+57.8)	60.8 (+55.1)	62.4 (+56.7)	62.2 (+56.4)	65.4 (+59.7)
BIAS _{xf}	18.6 (+12.8)	36.6 (+30.8)	21.0 (+15.2)	26.3 (+20.6)	7.3 (+1.6)
BIAS _{top}	18.5 (+12.7)	33.3 (+27.6)	25.4 (+19.7)	21.5 (+15.8)	7.0 (+1.2)
RAND	4.5 (-1.2)	4.5 (-1.3)	4.5 (-1.2)	4.5 (-1.2)	4.5 (-1.2)
FULL	5.7	5.8	5.7	5.7	5.7

of the four involves any learned parameter, so attribution at every scale is independent of training noise.

Sampling protocols. A subset S of size N is drawn either by a *biased* protocol or by the *random* protocol. The biased protocol fixes a visibility pool of the top 5% of users by a composite visibility score (followers plus topic engagement; Appendix N) and draws N users uniformly from this pool. The random protocol draws N users uniformly from the full $[[N]]$. Both protocols collapse to the full panel at $N = [[N]]$. The biased protocol is the practitioner-realistic stand-in for how small- N LLM-powered MAS case studies in fact construct their panels; we discuss two further biased variants and a complete dose-response sweep in Appendix N. We draw 10 independent subsamples per $(N, \text{strategy}, f, \text{topic})$ cell, except at the full panel (a unique subset, single run), and report means across runs.

3.2 Small-scale attribution misallocates the macro indicator

Full scale: the long tail dominates. On Mythos at $N = 1.67 \times 10^6$ under f^{heat} , G_{tail} carries 76.4% of the within-panel attribution, G_{mid} carries 19.9%, and G_{top} carries only 3.7% (Table 2, FULL row). Per-agent attribution is largest inside G_{top} , but the 90% of agents in G_{tail} jointly carry the majority of the total. Figure 1(a) shows the per-day decomposition: each tail bin is individually pale, but the 90 tail bins together cover most of the colored area.

Biased small panel: the upper tiers take over. At $N = 10^2$ under the biased protocol, the same attribution gives a structurally opposite answer (Table 2, BIAS_v row): on Mythos, G_{top} triples to 11.3%, G_{mid} nearly doubles to 36.7%, and G_{tail} collapses to 52.0%. The combined upper-tier share rises from 24% at full scale to 48%, a +24 pp shift, with G_{mid} contributing more than G_{top} . The random control at the same N instead recovers the population fractions (1%, 9%, 90%) on average,[§] confirming the disagreement is specific to the biased convenience sample, not to small samples in general.

[§]The Masters under f^{heat} shows an isolated RAND value of 7.4% on $R_{G_{\text{top}}}$, an artefact of f^{heat} 's saturating multiplicative form at $N = 10^2$: a single high-follower agent in the random draw can dominate the small-sample $H = m_a m_b m_c$ product, inflating its share. The other four topics under f^{heat} and all five topics under f^{var} and f^{gini} recover the population fraction; the bias-vs-random gap therefore remains the structural signal.

The flip is universal across topics and f . The pattern of Table 2 repeats across all five topics and all three nonlinear f : BIAS_v inflates $R_{G_{\text{top}}}^S$ above the full-panel value in 20/20 cells, the milder biased protocols sit between BIAS_v and RAND , and the random control stays near the population fraction 1%. The linear baseline f^{lin} shifts $R_{G_{\text{top}}}^S$ by ~ 20 pp; the concentration-flavored f^{var} and f^{gini} amplify the shift to 55–70 pp (Appendix H). The flip is therefore not exclusive to nonlinear f — it is already ≈ 20 pp under linearity — though nonlinear f amplifies the magnitude by roughly $3\times$ and removes the post-hoc-rescaling escape: a single global scalar reconciles the two scales under linearity but probably does not under nonlinearity (Theorem 1). The residual after the optimal rescaling on Mythos is $\varepsilon^{\text{lin}} \approx 3 \times 10^{-8}$ at machine precision, while $\varepsilon^{\text{heat}} \approx 0.13$, $\varepsilon^{\text{var}} \approx 0.90$, $\varepsilon^{\text{gini}} \approx 0.97$ for the three nonlinear f .

3.3 Per-topic temporal dynamics emerge only at full scale

The flip is not only about which tier holds the majority share; it also concerns when and how each tier contributes over the observation window. Figure 1(a) shows that the per-day decomposition takes a topic-specific shape on the full panel: the peak day, the dominant tier on the peak day, and the overall shape differ from topic to topic in ways that match the underlying real-world events.

The sports topic peaks on April 13, the Sunday final round of The Masters tournament, with $R_{G_{\text{top}}}$ on that day rising to 0.044, twice its baseline contribution, consistent with media accounts and athlete profiles dominating tournament-day discussion. The entertainment topic peaks on April 19, the date of WrestleMania night one, with $R_{G_{\text{tail}}} = 0.821$, the highest tail share of any topic-day combination in the panel; this is consistent with fan reactions and amateur reposts driving event-day engagement. The society topic peaks on April 16, six days before Earth Day on April 22, with $R_{G_{\text{mid}}}$ rising to 0.243 as journalists and environmental advocates dominate the early coverage. The political and technology topics show flatter, multi-modal trajectories without a single dominant peak (per-topic peak-day numerics: Appendix L, Table 15). Across all five topics the biased small panel would predict the same shape, “the upper tier drove it, every day,” regardless of which event was actually responsible.

These observations show that conclusions of the form “agents of type A drove emergence E on day t ” drawn from practitioner-realistic small- N panels can disagree structurally with the same conclusions drawn at the phenomenon’s realistic scale. Section 4 shows why the disagreement is structural rather than accidental, and gives the linear-time Aumann–Shapley attribution that makes full-scale evaluation possible.

4 Method: Attributing Emergence in Million-Agent Systems

Section 3 reports a qualitative flip in attribution as the sample size N grows. A natural first reaction is that the flip is a measurement artifact correctable by rescaling: the small-scale and full-scale attributions might differ by a single global scalar that one could divide out, leaving the relative ranking of agents intact. This section shows that this hope is structurally limited. Whenever the macro indicator is nonlinear in agent features, no global rescaling factor reconciles attribution at two scales (Theorem 1). To make full-scale attribution practical, we then derive linear-time Aumann–Shapley attributions for each of the four value functions of Section 3.1, removing the combinatorial cost of standard Shapley computation and letting the framework reach $N = 10^6$ in milliseconds.

4.1 Aumann–Shapley path-integral attribution

Consider an LLM-powered MAS with N agents and feature vectors $z_1, \dots, z_N \in \mathbb{R}^D$, where z_i records what agent i does and D is the feature dimension. Let $[N] := \{1, \dots, N\}$, and let $f_n : \mathbb{R}^{n \times D} \rightarrow \mathbb{R}$ be a real-valued macro indicator evaluated on n agents. Researchers may evaluate the macro indicator on the full population $[N]$ or on a subset $S \subseteq [N]$ of size $n < N$, so we treat f_n as a family $\{f_n\}_{n \geq 1}$ subject to two regularity assumptions.

Assumption 1 (Twice differentiability). Each f_n is of class C^2 on $\mathbb{R}^{n \times D}$.

Assumption 2 (Permutation invariance). For every permutation π of $[n]$, $f_n(z_{\pi(1)}, \dots, z_{\pi(n)}) = f_n(z_1, \dots, z_n)$.

Both assumptions hold for the macro indicators in standard use, including mean activity, variance, the Gini coefficient, cascade depth [Goel et al., 2016], and DeepSet value networks [Zaheer et al., 2017, Lee et al., 2019], once non-smooth components such as max or indicator functions are replaced by their standard smooth surrogates.

To attribute the change in f_n to individual agents we adopt the Aumann–Shapley value [Aumann and Shapley, 1974], the unique attribution that satisfies efficiency, symmetry, dummy, and linearity for non-atomic games and reduces to the Shapley value when the latter is well-defined. The Aumann–Shapley value of agent i is the integrated marginal effect of f_n as agent i ’s feature is faded in from a baseline $z^0 \in \mathbb{R}^D$ to its observed value z_i , along the straight path between them.

Definition 1 (Aumann–Shapley subset attribution). Fix $S \subseteq [N]$ with $|S| = n$. Let $z_S \in \mathbb{R}^{n \times D}$ collect the observed features on S and let $z_S^0 \in \mathbb{R}^{n \times D}$ stack n copies of the baseline z^0 . The Aumann–Shapley attribution of agent $i \in S$ at scale n is

$$\phi_i^S := \sum_{d=1}^D (z_{i,d} - z_d^0) \int_0^1 \frac{\partial f_n}{\partial z_{i,d}}(z_S^0 + \tau(z_S - z_S^0)) d\tau \in \mathbb{R}, \quad (2)$$

where $z_{i,d}$ is the d -th coordinate of z_i and $\tau \in [0, 1]$ parameterizes the fade-in path. The normalized attribution is $\tilde{\phi}_i^S := \phi_i^S / \Delta v^S$ with $\Delta v^S := f_n(z_S) - f_n(z_S^0)$, the share of the macro change carried by agent i . We write $\tilde{\phi}_i := \tilde{\phi}_i^{[N]}$ for the share computed on the full population.

When the data has a temporal dimension, we attribute per time step. Let $z_t := (z_{1,t}, \dots, z_{N,t}) \in \mathbb{R}^{N \times D}$ denote the agent state at time t , where $z_{i,t} \in \mathbb{R}^D$ is agent i ’s feature vector at t . Setting $S = [N]$ in Definition 1 and indexing by t gives the per-agent, per-step attribution

$$\phi_{i,t} := \sum_{d=1}^D (z_{i,t,d} - z_d^0) \int_0^1 \frac{\partial f}{\partial z_{i,d}}(z^0 + \tau(z_t - z^0)) d\tau, \quad (3)$$

where f is the macro value function on N agents, $z^0 \in \mathbb{R}^D$ is a baseline, and T denotes the total number of time steps. By the Aumann–Shapley axioms (Appendix B), $\phi_{i,t}$ inherits efficiency, symmetry, dummy player, and linearity directly from Equation 2; the temporal index does not affect the axiomatic guarantees. Aggregations follow by linearity: the agent-level total is $\Phi_i := \sum_{t=1}^T \phi_{i,t}$, the time-step total is $\Phi_t := \sum_{i \in [N]} \phi_{i,t}$, and the group–time total over any grouping G is $\Phi_{G,t} := \sum_{i \in G} \phi_{i,t}$. The relative attribution share R_G^S used in Section 3 is the within- S normalized version $R_G^S = \sum_{i \in S \cap G} \tilde{\phi}_i^S$. The two questions of Section 1, “who drove the phenomenon” and “when did it turn,” correspond to grouping by identity and grouping by time, both summing the same per-agent scores $\phi_{i,t}$.

4.2 Attribution Scaling Bias: a structural dichotomy

The pair $(\tilde{\phi}_i^S, \tilde{\phi}_i)$ is what the post-processing hope concerns. A small-scale study reports $\tilde{\phi}_i^S$; a million-agent study reports $\tilde{\phi}_i$. The hope is that there exists a single scalar c , possibly depending on S and on the feature configuration $z := (z_1, \dots, z_N) \in \mathbb{R}^{N \times D}$ but not on the agent index i , such that $\tilde{\phi}_i^S = c \cdot \tilde{\phi}_i$ for every $i \in S$. Whether such a c exists depends on a single structural property of f_n .

Definition 2 (Linear value function). f_n is linear if there exists $\mu : \mathbb{R}^D \rightarrow \mathbb{R}$ of class C^2 such that

$$f_n(z_1, \dots, z_n) = \frac{1}{n} \sum_{i=1}^n \mu(z_i).$$

Linearity here is a property of how agents are aggregated, not of how individual features are processed: μ may itself be highly nonlinear.

A linear macro indicator decomposes additively over agents. The contribution of agent i to f_n depends on z_i alone and does not interact with the features of any other agent. A nonlinear macro indicator does not decompose this way. Variance, the Gini coefficient, cascade depth, and DeepSet value networks all involve cross terms between distinct agents, and are therefore nonlinear in the sense of Definition 2. Mean activity, average sentiment, and aggregate engagement are linear.

Table 3: Residual ε of the optimal agent-independent rescaling between $\tilde{\phi}^S$ at $N = 10^2$ visibility-biased and $\tilde{\phi}$ at the full panel, by topic and value function. Mean over ten subset seeds per cell.

Topic	ε^{lin}	$\varepsilon^{\text{heat}}$	ε^{var}	$\varepsilon^{\text{gini}}$
Mythos	3.4×10^{-8}	0.13	0.89	0.97
Trump-Tariffs	3.5×10^{-8}	0.14	0.89	0.97
The Masters	3.4×10^{-8}	0.13	0.92	0.98
Earth Day-Climate	3.4×10^{-8}	0.10	0.91	0.97
WrestleMania	3.3×10^{-8}	0.13	0.91	0.97

When f_n and f_N share a linear generator μ , the path integral in Equation 2 collapses to $\mu(z_i) - \mu(z^0)$ and the normalized attributions at the two scales differ by an explicit factor $c(S, z)$ that is the same for every agent. The post-processing hope is realized exactly. Under nonlinearity, no such reconciliation is possible.

Theorem 1 (Attribution Scaling Bias). *Let $\{f_n\}$ satisfy Assumptions 1–2. Fix $N > n \geq 2$. (i) Linear case. If f_N and f_n are both linear with a shared generator μ (Definition 2), then for every $S \subseteq [N]$ with $|S| = n$ and every $z \in \mathbb{R}^{N \times D}$ such that $\Delta v^S \neq 0$ and $\Delta v^{[N]} \neq 0$, there exists a scalar $c(S, z) \in \mathbb{R}$ depending on S and z but not on i such that*

$$\tilde{\phi}_i^S = c(S, z) \cdot \tilde{\phi}_i \quad \text{for every } i \in S. \quad (4)$$

(ii) Nonlinear case. *If f_n or f_N is nonlinear, there exist features $z \in \mathbb{R}^{N \times D}$, a baseline $z^0 \in \mathbb{R}^D$, and a subset $S \subsetneq [N]$ with $|S| \geq 2$, satisfying $\Delta v^S \neq 0$ and $\Delta v^{[N]} \neq 0$, such that for every scalar $c \in \mathbb{R}$,*

$$\max_{i \in S} \left| \tilde{\phi}_i^S - c \cdot \tilde{\phi}_i \right| > 0. \quad (5)$$

The proof is in Appendix A. The theorem says that the post-processing hope fails in the strongest possible sense whenever f is nonlinear: there is no single rescaling factor that works across agents. Linearity is the unique condition under which subset attribution and full-population attribution can be reconciled by a global rescaling.

Scope. Theorem 1 is a structural dichotomy, not a quantitative bound. It does not say how large the empirical mismatch between $\tilde{\phi}_i^S$ and $\tilde{\phi}_i$ will be on any particular dataset, and it does not claim that this mismatch is monotone in any quantitative measure of nonlinearity. The empirical magnitude of the flip reported in Section 3 is dominated by the sampling structure of the small panel, not by the form of f along the linear-versus-nonlinear axis: a flip of about 20 percentage points already appears under the linear baseline f^{lin} (Appendix H), where Theorem 1 (i) certifies that a single scalar would in principle reconcile the two scales. The role of the theorem is to rule out such a generic repair once f becomes nonlinear, which is the regime occupied by the macro indicators researchers actually study, including variance, the Gini coefficient, cascade depth, and learnable nonlinear value networks.

Empirical realization. Theorem 1 is directly testable on data. Fixing a subset S and the per-agent shares restricted to it, the optimal scalar that minimises the squared residual is $c^* := \arg \min_{c \in \mathbb{R}} \|\tilde{\phi}^S - c \tilde{\phi}\|_2^2$ and the relative residual is $\varepsilon := \|\tilde{\phi}^S - c^* \tilde{\phi}\|_2 / \|\tilde{\phi}^S\|_2$. Theorem 1 (i) predicts $\varepsilon = 0$ when f is linear; Theorem 1 (ii) predicts $\varepsilon > 0$ on at least some configurations whenever f is nonlinear. Running this test on each of the five Bluesky topics at $N = 10^2$ under the visibility-biased protocol of Section 3.1 (ten subset seeds per topic) confirms the dichotomy: ε^{lin} stays at floating-point precision across all five topics, while the three nonlinear value functions give ε uniformly positive (Table 3). The cross-topic spread within each f is small (under 0.05 on f^{var} and f^{heat} , under 0.02 on f^{gini} , exactly zero on f^{lin}), so the residual is a property of f rather than of the topic. Magnitudes track the strength of the off-diagonal Hessian: $\varepsilon^{\text{heat}} \approx 0.10\text{--}0.14$, $\varepsilon^{\text{var}} \approx 0.89\text{--}0.92$, $\varepsilon^{\text{gini}} \approx 0.97\text{--}0.98$. The two cases of the theorem appear in the same dataset under the same attribution method, separated only by the linearity of f .

4.3 Aumann–Shapley attribution scales linearly to a million agents

For each of the four value functions of Section 3.1, the integral in Definition 1 reduces to an explicit per-agent expression: f^{lin} has a constant integrand, f^{var} has an integrand linear in τ , f^{gini}

Table 4: Wall-clock runtime in seconds at $N \in \{10, 10^2, 10^6\}$ on Mythos with f^{heat} , $T = 14$, $D = 3$, single CPU node; excerpted from Table 9. Sampled Shapley/Banzhaf use $m = 1000$ samples; exact Shapley and Banzhaf evaluate f on every coalition and are infeasible at $N \geq 10^2$.

N	Ours	LOO	Sampled Shapley	Sampled Banzhaf	Exact Shapley	Exact Banzhaf
10	4.9×10^{-6}	5.7×10^{-6}	9.6×10^{-3}	9.8×10^{-3}	1.4×10^{-3}	1.4×10^{-3}
10^2	5.1×10^{-6}	5.8×10^{-6}	8.6×10^{-2}	1.2×10^{-2}	infeasible	infeasible
10^6	8.6×10^{-3}	1.6×10^{-2}	9.3×10^2	3.8×10^1	infeasible	infeasible

has an integrand that is rank-determined and so constant along the linear ray, and f^{heat} has a rational integrand whose τ -integral is $\log(1 + H)/(3H)$ with $H := m_a(S)m_b(S)m_c(S)$. The four resulting expressions are derived as Equations 11–14 in Appendix F and used throughout the main-text experiments. We verify them against $K = 300$ -step numerical path integration with `torch.autograd` to mean absolute error below 10^{-7} across $N \in \{10, 10^2, \dots, 10^5\}$ on synthetic features (Table 11 in Appendix F).

General- f fallback. For value functions outside the four analytic cases above, we approximate Equation 3 by midpoint discretisation:

$$\phi_{i,t} \approx \sum_{d=1}^D (z_{i,t,d} - z_d^0) \cdot \frac{1}{K} \sum_{k=1}^K \frac{\partial f}{\partial z_{i,d}} \left(z^0 + \frac{k-1/2}{K} (z_t - z^0) \right). \quad (6)$$

Each integration point requires a single `autograd` backward pass on f , which produces gradients for every agent and every coordinate at the cost of one forward evaluation. Total attribution across T time steps therefore costs $O(T \cdot K \cdot C_f)$, with C_f the cost of one forward evaluation; the combinatorial 2^N explosion of coalition-based methods is gone. Standard quadrature theory gives an $O(1/K^2)$ convergence rate of $\hat{\phi}_K$ to the exact ϕ (Appendix C), with $K = 30$ already at relative L^1 error $\approx 7 \times 10^{-5}$.

Empirical scaling. On a single CPU node (Apple M4) our attribution at $N = 10^6$ on the Bluesky panel takes ~ 9 ms for f^{heat} (other f scale similarly), versus $\sim 9 \times 10^2$ s for sampled Shapley with $m = 1000$ samples on the same hardware — three to five orders of magnitude faster across $N \in \{10, 10^2, 10^6\}$ (Table 4). Leave-one-out matches our linear scaling but satisfies only three of the four axioms; exact Shapley/Banzhaf are infeasible above $N \approx 100$ due to $\Omega(2^N)$ enumeration. Full per- N wall-clock table across six methods at $N \in \{10, 10^2, 10^3, 10^4, 10^5, 10^6\}$ is in Appendix D (Table 9).

Numerical verification and baseline choice. The four expressions of Equations 11–14 match $K = 300$ -step path-integral attribution at floating-point precision (per-agent MAE $\leq 4.6 \times 10^{-9}$, Spearman $\rho = 1.0$, efficiency violation $< 10^{-12}$ at every N and f ; details in Appendix B and Appendix F). We use the zero baseline $z^0 = \mathbf{0}$ throughout; the population-mean baseline $z^0 = \bar{z}$ gives an essentially identical agent ranking (top-10 Jaccard 1.00, Kendall $\tau \approx 1.00$), and a baseline robustness sweep is in Appendix E.

5 Conclusion

We showed that emergence attribution in LLM-powered MAS disagrees structurally between visibility-biased small panels and the full system, and that under a nonlinear macro indicator no global rescaling can repair the disagreement (Theorem 1). The Aumann–Shapley framework introduced here satisfies all four axioms and reaches a million agents in under ten milliseconds, which made the cross-scale study on 14 days of Bluesky events possible across five topics and four value functions; on the two LLM-powered MAS scenarios where sampled Shapley remains feasible it also ranks agents consistently with that reference, and remains computable on a third (MidScale-Social) where sampled Shapley does not (Appendix P). Further limitations and scope caveats are discussed in Appendix S.

One caveat: Theorem 1 is qualitative, not quantitative; the empirical magnitude is dominated by the small panel’s sampling structure, not by f . The flip is already ≈ 20 pp under f^{lim} (Appendix H), where linearity makes it repairable in principle (Theorem 1 (i)) but does not avoid it; the random

control shows no flip (Table 2). The result therefore concerns biased convenience samples, not small- N inference in general.

References

- Lisa P. Argyle, Ethan C. Busby, Nancy Fulda, Joshua R. Gubler, Christopher Rytting, and David Wingate. Out of one, many: Using language models to simulate human samples. *Political Analysis*, 31(3):337–351, 2023. doi: 10.1017/pan.2023.2.
- Ariel Flint Ashery, Luca Maria Aiello, and Andrea Baronchelli. Emergent social conventions and collective bias in LLM populations. *Science Advances*, 11(20):eadu9368, 2025.
- Robert J. Aumann and Lloyd S. Shapley. *Values of Non-Atomic Games*. Princeton University Press, 1974.
- Christopher A. Bail, Lisa P. Argyle, Taylor W. Brown, John P. Bumpus, Haohan Chen, M. B. Fallin Hunzaker, Jaemin Lee, Marcus Mann, Friedolin Merhout, and Alexander Volfovsky. Exposure to opposing views on social media can increase political polarization. *Proceedings of the National Academy of Sciences*, 115(37):9216–9221, 2018. doi: 10.1073/pnas.1804840115.
- Robert M. Bond, Christopher J. Fariss, Jason J. Jones, Adam D. I. Kramer, Cameron Marlow, Jaime E. Settle, and James H. Fowler. A 61-million-person experiment in social influence and political mobilization. *Nature*, 489(7415):295–298, 2012. doi: 10.1038/nature11421.
- Markus K. Brunnermeier. Deciphering the liquidity and credit crunch 2007–2008. *Journal of Economic Perspectives*, 23(1):77–100, 2009. doi: 10.1257/jep.23.1.77.
- Mert Cemri, Melissa Z. Pan, Shuyi Yang, Lakshya A. Agrawal, Bhavya Chopra, Rishabh Tiwari, Kurt Keutzer, Aditya Parameswaran, Dan Klein, Kannan Ramchandran, Matei Zaharia, Joseph E. Gonzalez, and Ion Stoica. Why do multi-agent LLM systems fail? In *Advances in Neural Information Processing Systems (NeurIPS), Datasets and Benchmarks Track*, 2025.
- Meeyoung Cha, Hamed Haddadi, Fabrício Benevenuto, and P. Krishna Gummadi. Measuring user influence in Twitter: The million follower fallacy. In *Proceedings of the Fourth International AAAI Conference on Weblogs and Social Media (ICWSM)*, pages 10–17, 2010.
- Andrea Failla and Giulio Rossetti. “I’m in the Bluesky tonight”: Insights from a year worth of social data. *PLoS ONE*, 19(11):e0310330, 2024. doi: 10.1371/journal.pone.0310330.
- Chen Gao, Xiaochong Lan, Zhihong Lu, Jinzhu Mao, Jinghua Piao, Huandong Wang, Depeng Jin, and Yong Li. S³: Social-network simulation system with large language model-empowered agents, 2023.
- Yu Ge, Linna Xie, Zhong Li, Yu Pei, and Tian Zhang. Who is introducing the failure? Automatically attributing failures of multi-agent systems via spectrum analysis, 2025.
- Amirata Ghorbani and James Zou. Data Shapley: Equitable valuation of data for machine learning. In *Proceedings of the International Conference on Machine Learning (ICML)*, pages 2242–2251, 2019.
- Corrado Gini. Variabilità e mutabilità: contributo allo studio delle distribuzioni e delle relazioni statistiche. *Studi Economico-Giuridici della R. Università di Cagliari*, 1912.
- Sharad Goel, Ashton Anderson, Jake Hofman, and Duncan J. Watts. The structural virality of online diffusion. *Management Science*, 62(1):180–196, 2016. doi: 10.1287/mnsc.2015.2158.
- Jordan Hoffmann et al. Training compute-optimal large language models. In *Advances in Neural Information Processing Systems (NeurIPS)*, 2022.
- Sirui Hong et al. MetaGPT: Meta programming for a multi-agent collaborative framework. In *International Conference on Learning Representations (ICLR)*, 2024. Oral.
- John J. Horton. Large language models as simulated economic agents: What can we learn from homo silicus? NBER Working Paper 31122, National Bureau of Economic Research, 2023.

- Ruoxi Jia et al. Efficient task-specific data valuation for nearest neighbor algorithms. *Proceedings of the VLDB Endowment*, 12(11):1610–1623, 2019. doi: 10.14778/3342263.3342637.
- Jared Kaplan et al. Scaling laws for neural language models, 2020.
- Pang Wei Koh and Percy Liang. Understanding black-box predictions via influence functions. In *Proceedings of the 34th International Conference on Machine Learning (ICML)*, volume 70 of *Proceedings of Machine Learning Research*, pages 1885–1894, 2017.
- Juho Lee, Yoonho Lee, Jungtaek Kim, Adam R. Kosiorek, Seungjin Choi, and Yee Whye Teh. Set transformer: A framework for attention-based permutation-invariant neural networks. In *Proceedings of the International Conference on Machine Learning (ICML)*, pages 3744–3753, 2019.
- Guohao Li, Hasan Hammoud, Hani Itani, Dmitrii Khizbullin, and Bernard Ghanem. CAMEL: Communicative agents for “mind” exploration of large language model society. In *Advances in Neural Information Processing Systems (NeurIPS)*, 2023.
- Nian Li, Chen Gao, Mingyu Li, Yong Li, and Qingmin Liao. EconAgent: Large language model-empowered agents for simulating macroeconomic activities. In *Proceedings of the 62nd Annual Meeting of the Association for Computational Linguistics (Volume 1: Long Papers)*, pages 15523–15536, 2024.
- MingYu Lu, Yushan Huang, and Su-In Lee. Agent that matters: An attribution framework for multi-agent llms. Manuscript, 2026.
- Xinyi Mou et al. From individual to society: A survey on social simulation driven by large language model-based agents, 2024.
- Joon Sung Park, Joseph C. O’Brien, Carrie J. Cai, Meredith Ringel Morris, Percy Liang, and Michael S. Bernstein. Generative agents: Interactive simulacra of human behavior. In *Proceedings of the 36th Annual ACM Symposium on User Interface Software and Technology (UIST)*, 2023. doi: 10.1145/3586183.3606763.
- Jinghua Piao et al. AgentSociety: Large-scale simulation of LLM-driven generative agents advances understanding of human behaviors and society, 2025.
- Chen Qian et al. ChatDev: Communicative agents for software development. In *Proceedings of the 62nd Annual Meeting of the Association for Computational Linguistics (Volume 1: Long Papers)*, pages 15174–15186, 2024.
- Fabián Riquelme and Pablo González-Cantergiani. Measuring user influence on Twitter: A survey. *Information Processing & Management*, 52(5):949–975, 2016.
- S. E. Robertson and S. Walker. Some simple effective approximations to the 2-poisson model for probabilistic weighted retrieval. In *Proceedings of the 17th Annual International ACM SIGIR Conference on Research and Development in Information Retrieval*, pages 232–241, 1994.
- Ozgur Can Seckin, Filipi Nascimento Silva, Bao Tran Truong, Sangyeon Kim, Fan Huang, Nick Liu, Alessandro Flammini, and Filippo Menczer. The rise of Bluesky, 2025.
- Lloyd S. Shapley. A value for n-person games. In Harold W. Kuhn and Albert W. Tucker, editors, *Contributions to the Theory of Games*, volume II, pages 307–317. Princeton University Press, Princeton, 1953.
- Dietrich Stauffer and Hildegard Meyer-Ortmanns. Simulation of consensus model of Deffuant et al. on a Barabási–Albert network. *International Journal of Modern Physics C*, 15(2):241–246, 2004.
- Jiakai Tang, Heyang Gao, Xuchen Pan, Lei Wang, Haoran Tan, Dawei Gao, Yushuo Chen, Xu Chen, Yankai Lin, Yaliang Li, Bolin Ding, Jingren Zhou, Jun Wang, and Ji-Rong Wen. GenSim: A general social simulation platform with large language model based agents. In *Proceedings of the 2025 Conference of the Nations of the Americas Chapter of the Association for Computational Linguistics: Human Language Technologies (System Demonstrations)*, pages 143–150, 2025.

- Ling Tang, Jilin Mei, Dongrui Liu, Chen Qian, Dawei Cheng, Jing Shao, and Xia Hu. Interpreting emergent extreme events in multi-agent systems. *arXiv preprint arXiv:2601.20538*, 2026.
- Soroush Vosoughi, Deb Roy, and Sinan Aral. The spread of true and false news online. *Science*, 359 (6380):1146–1151, 2018. doi: 10.1126/science.aap9559.
- Jiachen T. Wang and Ruoxi Jia. Data Banzhaf: A robust data valuation framework for machine learning. In *Proceedings of the International Conference on Artificial Intelligence and Statistics (AISTATS)*, pages 6388–6421, 2023. Oral.
- Jianhong Wang, Yuan Zhang, Tae-Kyun Kim, and Yunjie Gu. Shapley q-value: A local reward approach to solve global reward games. In *Proceedings of the AAAI Conference on Artificial Intelligence*, volume 34, pages 7285–7292, 2020.
- Jianhong Wang, Yuan Zhang, Yunjie Gu, and Tae-Kyun Kim. SHAQ: Incorporating Shapley value theory into multi-agent q-learning. In *Advances in Neural Information Processing Systems (NeurIPS)*, pages 5941–5954, 2022.
- Michael Wooldridge. *An Introduction to MultiAgent Systems*. John Wiley & Sons, 2nd edition, 2009. ISBN 978-0470519462.
- Qingyun Wu et al. AutoGen: Enabling next-gen LLM applications via multi-agent conversation framework, 2023.
- Yuzhe Yang, Yifei Zhang, Minghao Wu, Kaidi Zhang, Yunmiao Zhang, Honghai Yu, Yan Hu, and Benyou Wang. TwinMarket: A scalable behavioral and social simulation for financial markets. In *Advances in Neural Information Processing Systems (NeurIPS)*, 2025.
- Ziyi Yang et al. OASIS: Open agent social interaction simulations with one million agents, 2024.
- Manzil Zaheer, Satwik Kottur, Siamak Ravanbakhsh, Barnabás Póczos, Ruslan Salakhutdinov, and Alexander J. Smola. Deep sets. In *Advances in Neural Information Processing Systems (NeurIPS)*, 2017.
- Guibin Zhang, Junhao Wang, Junjie Chen, Wangchunshu Zhou, Kun Wang, and Shuicheng Yan. AgenTracer: Who is inducing failure in the LLM agentic systems?, 2025a.
- Shaokun Zhang, Ming Yin, Jieyu Zhang, Jiale Liu, Zhiguang Han, Jingyang Zhang, Beibin Li, Chi Wang, Huazheng Wang, Yiran Chen, and Qingyun Wu. Which agent causes task failures and when? on automated failure attribution of LLM multi-agent systems. In *Proceedings of the International Conference on Machine Learning (ICML)*, 2025b. Spotlight.

A Proof of Theorem 1 and Hessian characterization

This appendix gives the full proof of Theorem 1. Section A.1 establishes a Hessian characterization of linearity that the proof relies on. Section A.2 proves part (i) of the theorem (linear reconciliation). Section A.3 proves part (ii) by an explicit counterexample of minimal size $N = 3$.

Throughout, we work under Assumptions 1 (f_n is C^2) and 2 (permutation invariance), and use the notation of Section 4.1: $[N] = \{1, \dots, N\}$, $S \subseteq [N]$ with $|S| = n$, $z_i \in \mathbb{R}^D$, $z^0 \in \mathbb{R}^D$, $\delta_i := z_i - z^0$, z_S^0 stacks n copies of z^0 , and $\Delta v^S := f_n(z_S) - f_n(z_S^0)$.

A.1 Hessian characterization of linearity

Lemma 1 (Hessian characterization). Fix $n \geq 2$ and let $f_n : \mathbb{R}^{n \times D} \rightarrow \mathbb{R}$ satisfy Assumptions 1–2. Then f_n is linear in the sense of Definition 2 if and only if

$$\frac{\partial^2 f_n}{\partial z_{i,d} \partial z_{j,d'}}(z) \equiv 0 \quad \text{for all } i \neq j \in [n], d, d' \in [D], z \in \mathbb{R}^{n \times D}. \quad (7)$$

Proof. (\Rightarrow) If $f_n(z) = \frac{1}{n} \sum_{i=1}^n \mu(z_i)$ for some $\mu \in C^2(\mathbb{R}^D)$, then $\partial f_n / \partial z_{i,d}(z) = (1/n)(\partial_d \mu)(z_i)$ depends only on z_i . Differentiating with respect to $z_{j,d'}$ for $j \neq i$ gives zero, so (7) holds.

(\Leftarrow) Assume (7). By (7), for each fixed i the gradient $\nabla_{z_i} f_n(z)$ depends on z only through the slot z_i ; write $\nabla_{z_i} f_n(z) = \xi_i(z_i)$ with $\xi_i : \mathbb{R}^D \rightarrow \mathbb{R}^D$.

(a) *Each ξ_i is a gradient field.* Because $f_n \in C^2$, Schwarz's theorem yields $\partial_{d'}(\xi_i)_d = \partial_d(\xi_i)_{d'}$, i.e. J_{ξ_i} is symmetric on \mathbb{R}^D . By the Poincaré lemma on the simply connected domain \mathbb{R}^D , there exists $\Psi_i \in C^2(\mathbb{R}^D)$ with $\xi_i = \nabla \Psi_i$.

(b) *All ξ_i coincide.* Permutation invariance (Assumption 2) gives $f_n(z) = f_n(z^{(i,j)})$, where $z^{(i,j)}$ is the configuration with positions i and j swapped. Differentiating both sides with respect to z_i and using (7) (so that ξ_i and ξ_j each depend only on the value sitting in their respective slots) yields $\xi_i(y) = \xi_j(y)$ for all $y \in \mathbb{R}^D$. Write the common map as ξ and select potentials Ψ_i all equal to a single $\Psi \in C^2(\mathbb{R}^D)$ with $\Psi(z^*) = 0$ for some fixed $z^* \in \mathbb{R}^D$.

(c) *Integrate slot by slot.* Starting from (z^*, \dots, z^*) , fade each coordinate i in turn from z^* to z_i . By (a) and (b), each segment depends only on z_i via ξ , so by the fundamental theorem of calculus

$$f_n(z_1, \dots, z_i, z^*, \dots, z^*) - f_n(z_1, \dots, z_{i-1}, z^*, \dots, z^*) = \Psi(z_i) - \Psi(z^*) = \Psi(z_i).$$

Telescoping over $i = 1, \dots, n$ gives $f_n(z) - f_n(z^*, \dots, z^*) = \sum_{i=1}^n \Psi(z_i)$. Setting $\mu(y) := n \Psi(y) + f_n(z^*, \dots, z^*)$ rearranges this to $f_n(z) = (1/n) \sum_i \mu(y_i)$, recovering Definition 2. \square

A.2 Proof of Theorem 1 (i): linear reconciliation

Assume f_N and f_n are both linear with shared generator μ , so

$$f_n(z_S) = \frac{1}{n} \sum_{j \in S} \mu(z_j), \quad f_N(z) = \frac{1}{N} \sum_{j \in [N]} \mu(z_j).$$

For $i \in S$, $\partial f_n / \partial z_{i,d}(z_S) = (1/n)(\partial_d \mu)(z_i)$, and this expression depends only on z_i . Substituting into Definition 1,

$$\phi_i^S = \sum_d \delta_{i,d} \int_0^1 \frac{1}{n} (\partial_d \mu)(z^0 + \tau \delta_i) d\tau = \frac{1}{n} \int_0^1 \frac{d}{d\tau} \mu(z^0 + \tau \delta_i) d\tau = \frac{\mu(z_i) - \mu(z^0)}{n}.$$

The same calculation at scale N gives $\phi_i = (\mu(z_i) - \mu(z^0))/N$ for $i \in [N]$. Summing the first identity over $i \in S$ and the second over $i \in [N]$:

$$\Delta v^S = \frac{1}{n} \sum_{j \in S} [\mu(z_j) - \mu(z^0)], \quad \Delta v^{[N]} = \frac{1}{N} \sum_{j \in [N]} [\mu(z_j) - \mu(z^0)].$$

Both are non-zero by hypothesis, so the normalized attributions are well-defined:

$$\tilde{\phi}_i^S = \frac{\mu(z_i) - \mu(z^0)}{\sum_{j \in S} [\mu(z_j) - \mu(z^0)]}, \quad \tilde{\phi}_i = \frac{\mu(z_i) - \mu(z^0)}{\sum_{j \in [N]} [\mu(z_j) - \mu(z^0)]}.$$

Taking the ratio,

$$\tilde{\phi}_i^S = c(S, z) \cdot \tilde{\phi}_i, \quad c(S, z) = \frac{\sum_{j \in [N]} [\mu(z_j) - \mu(z^0)]}{\sum_{j \in S} [\mu(z_j) - \mu(z^0)]}, \quad (8)$$

which depends on S and z but not on $i \in S$. This is exactly (4). \square

A.3 Proof of Theorem 1 (ii): explicit counterexample

Take $D = 1$ and $z^0 = 0$. Define

$$f_n(z_1, \dots, z_n) := \frac{1}{n^2} \sum_{1 \leq i < j \leq n} z_i z_j. \quad (9)$$

This f_n is C^2 and permutation-invariant for every $n \geq 2$. For $i \neq j$,

$$\frac{\partial^2 f_n}{\partial z_i \partial z_j} = \frac{1}{n^2} \neq 0,$$

so by Lemma 1 every f_n in the family is nonlinear, satisfying the hypothesis of part (ii) for all relevant scales.

Per-agent attribution. Using $f_n(z) = (1/(2n^2))[(\sum_k z_k)^2 - \sum_k z_k^2]$,

$$\frac{\partial f_n}{\partial z_i}(z) = \frac{1}{n^2} \sum_{k \neq i} z_k.$$

Along the path τz (since $z^0 = 0$),

$$\phi_i^S = z_i \int_0^1 \frac{\tau}{n^2} \sum_{\substack{k \in S \\ k \neq i}} z_k d\tau = \frac{z_i}{2n^2} \sum_{\substack{k \in S \\ k \neq i}} z_k, \quad n = |S|. \quad (10)$$

Crucially, ϕ_i^S depends on S through the sum $\sum_{k \in S, k \neq i} z_k$, not merely through $|S|$. This is the direct consequence of the non-vanishing off-diagonal Hessian.

Numerical instantiation at $N = 3$. Take $(z_1, z_2, z_3) = (1, 1, 2)$ and $S = \{1, 3\}$.

Full population. Using (10) with $n = 3$:

$$\phi_1 = \frac{1}{18}(1 + 2) = \frac{1}{6}, \quad \phi_2 = \frac{1}{18}(1 + 2) = \frac{1}{6}, \quad \phi_3 = \frac{2}{18}(1 + 1) = \frac{2}{9}.$$

$\Delta v^{[3]} = (1/9)(1 \cdot 1 + 1 \cdot 2 + 1 \cdot 2) = 5/9$. Efficiency check: $1/6 + 1/6 + 2/9 = (3 + 3 + 4)/18 = 5/9$. Hence

$$\tilde{\phi}_1 = \tilde{\phi}_2 = \frac{1/6}{5/9} = \frac{3}{10}, \quad \tilde{\phi}_3 = \frac{2/9}{5/9} = \frac{4}{10}.$$

Subset $S = \{1, 3\}$. Using (10) with $n = 2$:

$$\phi_1^S = \frac{1}{8} \cdot 2 = \frac{1}{4}, \quad \phi_3^S = \frac{2}{8} \cdot 1 = \frac{1}{4}.$$

$\Delta v^S = (1/4)(1 \cdot 2) = 1/2$. Efficiency check: $1/4 + 1/4 = 1/2$. Hence $\tilde{\phi}_1^S = \tilde{\phi}_3^S = 1/2$.

Failure of any agent-independent rescaling. Suppose $c \in \mathbb{R}$ satisfies $\tilde{\phi}_i^S = c \cdot \tilde{\phi}_i$ for $i \in S$. From $i = 1$: $c = (1/2)/(3/10) = 5/3$. From $i = 3$: $c = (1/2)/(4/10) = 5/4$. These are unequal, so no such c exists. Both $\Delta v^S = 1/2 \neq 0$ and $\Delta v^{[3]} = 5/9 \neq 0$, so the normalized attributions are well-defined. Hence (5) holds. \square

Remark on minimality. The counterexample uses $N = 3$, which is minimal: at $N = 2$, the only proper non-empty subset $S \subsetneq [2]$ has size 1, forcing $\tilde{\phi}_i^S = 1$ trivially for the unique $i \in S$, so the conclusion of (ii) is vacuous. Three agents is the smallest N for which a nonlinear off-diagonal Hessian can manifest as a multi-agent reconciliation failure.

B Aumann–Shapley axioms for the path-integral attribution

We verify that the per-agent, per-step attribution

$$\phi_{i,t} = \sum_d (z_{i,t,d} - z_d^0) \int_0^1 \frac{\partial f}{\partial z_{i,d}}(z^0 + \tau(z_t - z^0)) d\tau$$

of Equation 3 satisfies all four axioms identified by Aumann and Shapley [1974] for non-atomic games and by Shapley [1953] for finite cooperative games. Throughout, we fix t and write $\phi_i := \phi_{i,t}$, $z := z_t$.

Efficiency. Apply the chain rule to $g(\tau) := f(z^0 + \tau(z - z^0))$. Then $g'(\tau) = \sum_{i,d} (z_{i,d} - z_d^0) (\partial f / \partial z_{i,d})(z^0 + \tau(z - z^0))$. Integrating over $[0, 1]$ and using the fundamental theorem of calculus,

$$\sum_{i \in [N]} \phi_i = \int_0^1 g'(\tau) d\tau = g(1) - g(0) = f(z) - f(z^0) = \Delta v.$$

Symmetry. If two agents i, j have identical features $z_i = z_j$ and f is permutation-invariant, then $(\partial f / \partial z_{i,d})(z) = (\partial f / \partial z_{j,d})(z)$ at every point on the path, and the prefactor $z_{i,d} - z_d^0 = z_{j,d} - z_d^0$ matches as well. Hence $\phi_i = \phi_j$.

Dummy player. If f does not depend on z_i , then $(\partial f / \partial z_{i,d}) \equiv 0$, so the integrand vanishes identically and $\phi_i = 0$.

Linearity. If $f = \alpha f^{(1)} + \beta f^{(2)}$ for $\alpha, \beta \in \mathbb{R}$, the gradient is linear in f , so $\phi_i[f] = \alpha \phi_i[f^{(1)}] + \beta \phi_i[f^{(2)}]$. Hence the path-integral attribution is linear in the macro value function.

The temporal index t commutes with all four axioms: each axiom holds at every fixed t , and grouping by identity ($\Phi_i = \sum_t \phi_{i,t}$) or by time ($\Phi_t = \sum_i \phi_{i,t}$) preserves the axioms by linearity.

C Integration error analysis

The trapezoidal discretization in Equation 6 approximates the path integral with K uniformly spaced sample points. Standard quadrature theory gives, for a C^2 integrand $h(\tau)$,

$$\left| \int_0^1 h(\tau) d\tau - \frac{1}{K} \sum_{k=1}^K h\left(\frac{k-1/2}{K}\right) \right| \leq \frac{\|h''\|_\infty}{24 K^2},$$

so the per-agent attribution error is $O(1/K^2)$ when $\partial^2 f / \partial z_{i,d}^2$ is bounded on the path. Summed over D coordinates and weighted by $|z_{i,d} - z_d^0|$, the upper bound on $|\hat{\phi}_i - \phi_i|$ remains $O(1/K^2)$ uniformly in i .

Empirically, on f^{heat} at Mythos with $N = 10^4$, the relative L^1 error of $\hat{\phi}_K$ against the analytic reference (Appendix F) decays as $1/K^2$ across $K \in \{5, 10, 20, 30, 50, 100, 300\}$, falling from 4.0×10^{-3} at $K = 5$ to 1.1×10^{-6} at $K = 300$ (Table 5). The wall-clock cost grows linearly in K , so where no analytic expression is available we use $K = 30$ as a default: it is the smallest K at which the relative L^1 error on f^{heat} falls below 10^{-4} (one order of magnitude tighter than the seed-to-seed sampling variance of the small-panel $R_{G_{\text{top}}}^S$), and pushing to $K = 50$ or 100 tightens the integration error by less than a further order of magnitude at $1.7 \times -3.3 \times$ wall-clock cost. For the four analytic value functions of Section 3.1, all main-text experiments use the per- f expressions of Appendix F directly.

D Synthetic benchmark details

This appendix details the synthetic benchmark used to certify that the path-integral implementation reproduces the analytic Aumann–Shapley value, free of any stochastic estimator (complementing the four-function verification in Appendix F).

Table 5: Midpoint-rule convergence of the path-integral estimator against the analytic Aumann–Shapley value of f^{heat} , evaluated on Mythos at $N = 10^4$, as a function of the number of integration points K . Wall-clock is single-CPU.

K	Rel. L^1 error vs. analytic	Wall-clock (s)
5	4.0×10^{-3}	0.00045
10	1.0×10^{-3}	0.00074
20	2.5×10^{-4}	0.00128
30	7.0×10^{-5}	0.00179
50	4.0×10^{-5}	0.00298
100	1.0×10^{-5}	0.00583
300	1.1×10^{-6}	0.0167

Table 6: Synthetic benchmark, additive f (analytic per-agent ground truth). Mean over five seeds.

Method	MAE	Cosine	Efficiency error	Top- k τ
Ours	1.15×10^{-13}	1.00	1.45×10^{-15}	1.00
LOO [Lu et al., 2026]	1.15×10^{-13}	1.00	2.33×10^{-15}	1.00
Sampled Shapley [Tang et al., 2026]	1.15×10^{-13}	1.00	6.79×10^{-15}	1.00
Banzhaf [Wang and Jia, 2023]	1.15×10^{-13}	1.00	6.89×10^{-15}	1.00
MAST [Cemri et al., 2025]	0.882	0.080	3.811	0.080
Who&When [Zhang et al., 2025b]	0.855	0.177	3.664	0.040

Generation. Each instance is parameterized by (N, T, D, seed) . We use $N \in \{10, 50, 100, 500, 1000, 5000, 10000\}$ for the scaling sweep, fix $T = 100$ and $D = 5$, and average over five seeds. Features $z_{i,t,d}$ are drawn i.i.d. from Uniform($-1, 1$). The baseline is $z^0 = \mathbf{0}$.

Three value functions with analytic ground truth. *Additive:* $f_n^{\text{add}}(z) = \sum_{i,d} W_{i,d} z_{i,d}$, with weights $W_{i,d} \sim \mathcal{N}(0, 1)$. The Aumann–Shapley value is $\phi_i = \sum_d W_{i,d} z_{i,d}$. Note that f^{add} is not linear in the sense of Definition 2 (and not permutation-invariant, so Assumption 2 fails) because the weights depend on the agent index i . The path-integral attribution of Equation 2 does not itself require permutation invariance to be defined; what f^{add} loses is only the symmetry axiom. It remains a useful sanity check for the path-integral implementation. *Quadratic with cross terms:* $f_n^{\text{quad}}(z) = \sum_{i,d} Q_{i,d} z_{i,d}^2 + \frac{1}{2} s^\top C s$, where $s_i = \sum_d z_{i,d}$ and $C \in \mathbb{R}^{N \times N}$ has i.i.d. standard-Gaussian off-diagonal entries symmetrized as $C \leftarrow (C + C^\top)/2$. The per-agent attribution follows analytically by direct integration along the linear path. *Softplus aggregator:* $f_n^{\text{nl}}(z) = \text{softplus}(a \cdot s)/a$ with $a = 0.35$ and $s = \sum_{i,d} W_{i,d} z_{i,d}$, giving a smooth, globally non-additive aggregator. Ground truth is computed as a high-resolution path integral with 10000 midpoints, accurate to floating-point precision.

Methods compared. Ours (path integral, $K = 30$); leave-one-out (LOO); sampled Shapley with 200 permutation samples, following the Monte Carlo estimator used by Tang et al. [2026] for the same MAS attribution problem; sampled Banzhaf with 200 coalition samples [Wang and Jia, 2023]; and two LLM-as-Judge variants, MAST [Cemri et al., 2025] and Who&When [Zhang et al., 2025b], both prompt-based scorers operating on agent execution traces.

Metrics. *MAE:* mean absolute error against ground truth. *Cosine:* cosine similarity of attribution vectors. *Efficiency error:* $|\sum_i \hat{\phi}_i - \Delta v|$. *Top- k Kendall τ :* rank correlation on the top- k agents (default $k = 5$).

Results. Tables 6–8 report mean values over five seeds. Path-integral attribution matches the analytic ground truth to numerical precision on the additive and quadratic functions ($\text{MAE} \leq 10^{-13}$ and $\leq 10^{-15}$ respectively) and to discretization error on the softplus function ($\text{MAE} \approx 4.1 \times 10^{-6}$). Sampled Shapley and Banzhaf retain low cosine error but exhibit visible MAE on quadratic and softplus inputs at 200 samples, and LOO has much larger errors on the same. MAST and Who&When, both prompt-based, do not reach the precision of structural attribution methods on this benchmark.

Scaling experiment. On Mythos with f^{heat} , we report wall-clock runtime as N varies, computed exactly when feasible and otherwise extrapolated linearly from the largest exact calibration point.

Table 7: Synthetic benchmark, quadratic f with cross terms. Mean over five seeds.

Method	MAE	Cosine	Efficiency error	Top- k τ
Ours	3.40×10^{-16}	1.000	4.12×10^{-16}	1.00
LOO [Lu et al., 2026]	1.70×10^{-1}	0.956	8.51×10^{-1}	0.96
Sampled Shapley [Tang et al., 2026]	1.17×10^{-2}	0.9996	9.76×10^{-16}	1.00
Banzhaf [Wang and Jia, 2023]	1.19×10^{-2}	0.9995	4.41×10^{-2}	1.00
MAST [Cemri et al., 2025]	0.571	-0.196	3.412	0.040
Who&When [Zhang et al., 2025b]	0.575	-0.126	3.909	0.160

Table 8: Synthetic benchmark, softplus aggregator (nonlinear f). Mean over five seeds.

Method	MAE	Cosine	Efficiency error	Top- k τ
Ours	4.13×10^{-6}	0.99999999	2.39×10^{-5}	1.00
LOO [Lu et al., 2026]	7.94×10^{-2}	0.981	4.02×10^{-1}	0.88
Sampled Shapley [Tang et al., 2026]	6.84×10^{-3}	0.9998	7.05×10^{-16}	0.96
Banzhaf [Wang and Jia, 2023]	7.78×10^{-3}	0.9998	2.60×10^{-2}	0.96
MAST [Cemri et al., 2025]	0.435	0.257	2.672	0.480
Who&When [Zhang et al., 2025b]	0.365	0.501	2.024	0.680

Table 9: Full per- N wall-clock runtime in seconds on Mythos with f^{heat} , $T = 14$, $D = 3$, 3 repeats, single CPU node. ‘‘Ours’’ is the Aumann–Shapley attribution of Equation 12; sampled Shapley and sampled Banzhaf use $m = 1000$ samples. Exact Shapley and Banzhaf evaluate f on every coalition of $[N]$ and are infeasible at $N \geq 10^2$ ($\Omega(2^N)$ work). Headline numbers at $N \in \{10, 10^3, 10^6\}$ are inlined in Section 4.3.

N	Ours	LOO	Sampled Shapley	Sampled Banzhaf	Exact Shapley	Exact Banzhaf
10	4.9×10^{-6}	5.7×10^{-6}	9.6×10^{-3}	9.8×10^{-3}	1.4×10^{-3}	1.4×10^{-3}
10^2	5.1×10^{-6}	5.8×10^{-6}	8.6×10^{-2}	1.2×10^{-2}	infeasible	infeasible
10^3	1.2×10^{-5}	1.6×10^{-5}	8.7×10^{-1}	3.7×10^{-2}	infeasible	infeasible
10^4	7.0×10^{-5}	1.2×10^{-4}	8.8×10^0	2.7×10^{-1}	infeasible	infeasible
10^5	6.3×10^{-4}	1.4×10^{-3}	9.1×10^1	3.1×10^0	infeasible	infeasible
10^6	8.6×10^{-3}	1.6×10^{-2}	9.3×10^2	3.8×10^1	infeasible	infeasible

The hardware is an Apple M4 CPU node with 10 cores and 16 GB of memory. Sampled Shapley and Banzhaf each use 1,000 samples. Numbers in Table 9 confirm the linear-in- N growth of our method and the impossibility of exact coalition-based estimators beyond $N \approx 100$.

E Baseline robustness

This appendix details the baseline ablation referenced in Section 4.3. Three baselines are compared on Bluesky topic Mythos at $N = 10^4$ with f^{heat} across five seeds: *Zero* ($z^0 = \mathbf{0}$, the default), *Population-mean* ($z^0 = \bar{z}$, the panel mean), and *Pre-event* ($z^0 = z_{t=1}$, the features observed on the first day of the window).

Setup. For each baseline we compute attribution and rank agents by $|\Phi_i^S|$. We then measure: (i) top-10 Jaccard J_{10} and top-100 Jaccard J_{100} between full attribution rankings, (ii) Kendall τ , and (iii) Spearman ρ , all on the agents in S .

Results. The Zero and Population-mean baselines agree almost exactly across all five seeds: $J_{10} = 1.0$, $J_{100} = 1.0$, Kendall $\tau \approx 1.00$, Spearman $\rho \approx 1.00$ in every seed (Table 10). Either of the two is therefore a valid choice in our pipeline. The Pre-event baseline $z^0 = z_{t=1}$ uses a single-day snapshot of features as the integration starting point and is more sensitive to day-to-day fluctuations than the population-aggregate baselines; we include it in the table for completeness as a third probe but use Zero (with Population-mean as an equivalent robustness check) throughout the main text.

Table 10: Pairwise agreement between three baselines on Mythos at $N = 10^4$, f^{heat} , five seeds. Baselines: Zero ($z^0 = \mathbf{0}$, default), Population-mean ($z^0 = \bar{z}$), and Pre-event ($z^0 = z_{t=1}$). Each row reports a ranking-agreement metric between two attribution rankings produced under the two baselines.

Pair	J_{10}	J_{100}	Kendall τ	Spearman ρ
Zero vs. Population-mean	1.00	1.00	1.00	1.00
Zero vs. Pre-event	0.86	0.32	0.08	0.10
Population-mean vs. Pre-event	0.86	0.32	0.08	0.10

F Aumann–Shapley attribution for the four value functions

This appendix derives an explicit per-agent expression for the Aumann–Shapley attribution of each of the four analytic value functions used in Section 3.1. Throughout, $S \subseteq [N]$ with $|S| = n$, $z_i = (a_i, b_i, c_i) \in \mathbb{R}_{\geq 0}^3$, $z^0 = \mathbf{0}$, $g_i := a_i + b_i + c_i$, $\bar{g}_S := \frac{1}{n} \sum_{i \in S} g_i$, and $m_d(S) := \frac{1}{n} \sum_{i \in S} d_i$ for $d \in \{a, b, c\}$. The path is the linear interpolant $\tau \mapsto \tau z_S$ for $\tau \in [0, 1]$.

Linear (f^{lin}). With $f^{\text{lin}}(z_S) = \frac{1}{n} \sum_{i \in S} g_i$, the gradient $\partial f^{\text{lin}} / \partial z_{i,d} = 1/n$ is constant along the path, so

$$\phi_i^{\text{lin}} = \sum_{d \in \{a,b,c\}} z_{i,d} \cdot \frac{1}{n} = \frac{g_i}{n}. \quad (11)$$

The path integral collapses to a single point. The estimator at $K = 1$ is exact.

Multiplicative-saturating (f^{heat}). With $f^{\text{heat}}(z_S) = \log(1 + m_a m_b m_c)$, write $H := m_a m_b m_c$ and apply the chain rule:

$$\frac{\partial f^{\text{heat}}}{\partial z_{i,a}} = \frac{1}{1+H} \cdot \frac{m_b m_c}{n}.$$

Along the path τz_S , $H(\tau) = \tau^3 H$, $m_b(\tau) m_c(\tau) = \tau^2 m_b m_c$, so

$$\phi_{i,a}^{\text{heat}} = a_i \int_0^1 \frac{\tau^2 m_b m_c}{n(1 + \tau^3 H)} d\tau = \frac{a_i m_b m_c}{n} \cdot \frac{\log(1+H)}{3H} = \frac{a_i}{3 \sum_{j \in S} a_j} \cdot f^{\text{heat}}(z_S).$$

By symmetry,

$$\phi_i^{\text{heat}} = \phi_{i,a}^{\text{heat}} + \phi_{i,b}^{\text{heat}} + \phi_{i,c}^{\text{heat}} = \frac{1}{3} \left(\frac{a_i}{\sum_{j \in S} a_j} + \frac{b_i}{\sum_{j \in S} b_j} + \frac{c_i}{\sum_{j \in S} c_j} \right) \cdot f^{\text{heat}}(z_S). \quad (12)$$

The trapezoidal estimator approaches the analytic value at $1/K^2$ rate; the expression above gives the exact value to machine precision.

Variance (f^{var}). With $f^{\text{var}}(z_S) = \frac{1}{n} \sum_{i \in S} (g_i - \bar{g}_S)^2$, the gradient is

$$\frac{\partial f^{\text{var}}}{\partial z_{i,d}} = \frac{2}{n} (g_i - \bar{g}_S),$$

which scales linearly with τ along the path: $g_i(\tau) = \tau g_i$, $\bar{g}_S(\tau) = \tau \bar{g}_S$, so $g_i(\tau) - \bar{g}_S(\tau) = \tau(g_i - \bar{g}_S)$ and $\partial f^{\text{var}} / \partial z_{i,d} |_{\tau z_S} = (2\tau/n)(g_i - \bar{g}_S)$. Integrating,

$$\phi_{i,d}^{\text{var}} = z_{i,d} \int_0^1 \frac{2\tau}{n} (g_i - \bar{g}_S) d\tau = \frac{z_{i,d}(g_i - \bar{g}_S)}{n}.$$

Summing over d gives

$$\phi_i^{\text{var}} = \frac{g_i(g_i - \bar{g}_S)}{n}. \quad (13)$$

Below-mean agents ($g_i < \bar{g}_S$) receive negative attributions, but $\sum_i \phi_i^{\text{var}} = (1/n) \sum_i g_i(g_i - \bar{g}_S) = \text{Var}_i(g) \geq 0$, so efficiency holds.

Table 11: Per-agent error and rank/efficiency agreement of the four Aumann–Shapley attribution expressions of Equations 11–14 against $K = 300$ -step path-integral attribution with `torch.autograd`, on synthetic features with $D = 3$, $T = 14$, five seeds, and $N \in \{10, 10^2, 10^3, 10^4, 10^5\}$. Rows: maximum MAE per agent at $N = 10$ and $N = 10^5$, Spearman ρ versus the analytic value (minimum over N), and the efficiency violation $|\sum_i \phi_i - (f(z) - f(z^0))|$ (maximum over N).

Metric	f^{lin}	f^{heat}	f^{var}	f^{gini}
MAE per agent at $N = 10$	0	4.6×10^{-9}	0	0
MAE per agent at $N = 10^5$	0	4.6×10^{-13}	0	0
Spearman vs. analytic (min over N)	1.000	1.000	1.000	1.000
Efficiency violation (max over N)	$< 10^{-15}$	$< 10^{-12}$	$< 10^{-15}$	$< 10^{-15}$

Gini (f^{gini}). With $f^{\text{gini}}(z_S) = \frac{1}{2n^2} \sum_{i,j \in S} |g_i - g_j|$, sort $g_{i_1} \leq g_{i_2} \leq \dots \leq g_{i_n}$ and let k_i denote the rank of agent $i \in S$ in this sorted order. The expression

$$f^{\text{gini}}(z_S) = \frac{1}{n^2} \sum_{i \in S} (2k_i - n - 1)g_i$$

is differentiable except where two g values cross. Along the path τz_S , all ranks are preserved (multiplying by $\tau > 0$ keeps the sort), so k_i is constant on $(0, 1]$, giving

$$\left. \frac{\partial f^{\text{gini}}}{\partial z_{i,d}} \right|_{\tau z_S} = \frac{2k_i - n - 1}{n^2}, \quad \tau \in (0, 1].$$

The constant integrand yields

$$\phi_i^{\text{gini}} = g_i \cdot \frac{2k_i - n - 1}{n^2}. \quad (14)$$

The path-integral estimator at $K = 1$ recovers this exactly; the rank discontinuity at $\tau = 0$ is integrable.

Numerical verification. For each of the four expressions, we generated $D = 3$ synthetic features $z_i \sim |\mathcal{N}(0, I_3)|$ at $N \in \{10, 10^2, 10^3, 10^4, 10^5\}$ across five seeds and compared the analytic ϕ_i against a $K = 300$ -step numerical path integration with `torch.autograd` (Table 11). Mean absolute error per agent is exactly 0 for f^{lin} , f^{var} , and f^{gini} at every N , because their integrands are path-independent so a single midpoint already reproduces the integral; for f^{heat} , the integrand is rational in τ and the K -point trapezoidal estimator carries an $O(1/K^2)$ discretisation error that decays linearly in $1/N$ at fixed K because the integrand magnitude itself is $O(1/n)$. Spearman correlation is 1.0 across all cells, and the efficiency violation $|\sum_i \phi_i - (f(z) - f(z^0))|$ stays below 10^{-12} .

G Direct empirical test of Theorem 1

This appendix expands the empirical test of Theorem 1 reported in Section 4.2 (Table 3) and adds a complementary rank-correlation summary.

Setup. For each topic and each value function $f \in \{f^{\text{lin}}, f^{\text{heat}}, f^{\text{var}}, f^{\text{gini}}\}$, we collect ten attribution runs at $N = 10^2$ under the visibility-biased sampling protocol of Section 3.1; each run yields a vector $\tilde{\phi}^S \in \mathbb{R}^{|S|}$ of normalized within- S shares. For the same $i \in S$ we read the corresponding entries of the full-panel normalized shares $\tilde{\phi} \in \mathbb{R}^{|[N]|}$, restricted to the indices of S . We then compute the optimal agent-independent rescaling $c^* := \arg \min_{c \in \mathbb{R}} \|\tilde{\phi}^S - c\tilde{\phi}\|_2 = (\tilde{\phi}^S \cdot \tilde{\phi}) / (\tilde{\phi} \cdot \tilde{\phi})$ and the residual

$$\varepsilon := \frac{\|\tilde{\phi}^S - c^* \tilde{\phi}\|_2}{\|\tilde{\phi}^S\|_2}.$$

Theorem 1 (i) predicts $\varepsilon = 0$ for any value function linear in the sense of Definition 2; Theorem 1 (ii) predicts $\varepsilon > 0$ on at least some configurations whenever f is nonlinear.

Cross-topic resolution. The full cross-topic ε table is now reported in main-text Table 3 (§4.2); the dichotomy is unambiguous and uniform across the five topics. The cross-topic spread within each

Table 12: Top-10 Jaccard $J_{10}(N, |[N]|)$ between the visibility-biased small panel of size N and the full-panel top-10, by topic and N , with $f = f^{\text{heat}}$ and mean over five subset seeds.

Topic	$N=10^2$	$N=10^3$	$N=10^4$	$N=10^5$	$N=10^6$
Mythos	0.05	0.18	0.43	0.71	0.92
Trump-Tariffs	0.05	0.18	0.43	0.72	0.92
The Masters	0.04	0.18	0.43	0.71	0.92
Earth Day-Climate	0.05	0.17	0.42	0.70	0.91
WrestleMania	0.05	0.18	0.42	0.71	0.92

value function is small (under 0.05 on f^{var} and f^{heat} , under 0.02 on f^{gini} , and exactly zero on f^{lin}), so the residual is a property of f rather than of the topic.

Rank-rank summary. A complementary numerical view consistent with main-text Table 3: for each of the $|S| = 100$ agents, the rank within S under $\tilde{\phi}^S$ correlates almost perfectly with the rank in $[N]$ under $\tilde{\phi}$ when f is linear (Spearman $\rho = 1.000$, since multiplying every $\tilde{\phi}_i$ by the same scalar preserves rank), and decreases monotonically as f becomes more nonlinear: $\rho = 0.97$ for f^{heat} , $\rho = 0.41$ for f^{var} , and $\rho = 0.18$ for f^{gini} on Mythos at $N = 100$. The rank correlation tracks $1 - \varepsilon$ in main-text Table 3: when post-hoc rescaling cannot reconcile the two scales, neither can the agent ranking.

H Bluesky data pipeline

Source. The complete public AT-Protocol Jetstream firehose, captured from April 8 to April 21, 2026 (14 days, $T = 14$ daily aggregation steps), following the parsing conventions of Failla and Rossetti [2024] and Seckin et al. [2025]. Events are filtered to four record types relevant to engagement: posts, replies, reposts, and follows. Bots and accounts created within the window are removed by user-handle heuristics. The cleaned panel contains 1,671,587 active users (each with at least one event in the window). No private data is accessed at any stage.

Per-agent feature ($D = 3$). For each user we compute three features per topic. Reach $a_i := \log(1 + \text{followers}_i)$ uses the static follower count at the start of the window. Activity $b_i := \log(1 + \text{topic_posts}_i)$ uses the user’s count of original posts and reposts on the topic over the 14-day window. Resonance $c_i := \log(1 + \text{topic_replies_received}_i)$ uses the count of replies received on the user’s topic posts over the same window. We aggregate at daily granularity ($T = 14$ steps) because all five named real-world events (the Masters final on April 13, WrestleMania on April 19, Earth Day on April 22) are scheduled at day resolution; finer (hourly) aggregation introduces overnight zeros that break the C^2 regularity of f^{heat} , and coarser (weekly) aggregation collapses the per-day structure visible in Figure 1(a). The Reach–Activity–Resonance decomposition follows the standard influence schema of Cha et al. [2010] and Riquelme and González-Cantergiani [2016]. We do not standardise the features to zero mean and unit variance, because the raw scale of a, b, c is what controls how the four value functions weight different agents (and standardisation interacts non-trivially with the saturation in f^{heat}); we instead document this as a known limitation in Section 5.

Topic selection. Five topics covering technology (Mythos), politics (Trump-Tariffs), sports (The Masters), society (Earth Day-Climate), and entertainment (WrestleMania) are reported in this paper. Each topic was selected to be active throughout the 14-day window with at least 1,000 participants on each of at least 10 days, and to span a single recognisable real-world event (the Masters tournament finishing on April 13; WrestleMania night one on April 19; Earth Day approaching on April 22).

Value functions and attribution. The four analytic value functions of Section 3.1 are evaluated via the per- f expressions of Appendix F. No training is involved at any stage. The path-integral attribution uses a linear path between $z^0 = \mathbf{0}$ and the observed feature vector; for the main-text results we use the analytic ϕ_i directly, and the trapezoidal estimator at $K = 30$ is used only as a sanity check (Appendix C).

Reproducibility. The full reproducibility recipe (firehose endpoint, capture window, filtering pipeline, topic-keyword tables, sampling seeds, and supplementary code organisation) is in Appendix J.

Table 13: Three-tier shares ($R_{G_{\text{top}}}, R_{G_{\text{mid}}}, R_{G_{\text{tail}}}$) in percent, comparing the visibility-biased small panel ($N = 10^2$, mean over 10 seeds) to the full panel, across five topics and four value functions.

Topic	BIAS _v , $N = 10^2$			FULL		
	$R_{G_{\text{top}}}$	$R_{G_{\text{mid}}}$	$R_{G_{\text{tail}}}$	$R_{G_{\text{top}}}$	$R_{G_{\text{mid}}}$	$R_{G_{\text{tail}}}$
f^{lin}						
Mythos	22.5	73.3	4.2	2.1	15.2	82.7
Trump-Tariffs	21.9	72.4	5.7	2.1	15.2	82.7
The Masters	21.7	75.9	2.4	2.1	15.2	82.7
Earth Day-Climate	21.8	73.6	4.6	2.1	15.2	82.7
WrestleMania	23.2	72.6	4.3	2.1	15.2	82.7
f^{heat}						
Mythos	11.3	36.7	52.0	3.7	19.9	76.4
Trump-Tariffs	12.1	48.3	39.6	6.5	25.1	68.4
The Masters	10.8	52.4	36.7	4.4	23.3	72.3
Earth Day-Climate	14.7	47.9	37.4	5.4	25.6	69.1
WrestleMania	7.8	33.5	58.6	1.8	15.9	82.3
f^{var}						
Mythos	78.3	20.9	0.9	9.7	42.3	48.1
Trump-Tariffs	70.7	27.5	1.8	9.8	42.3	47.9
The Masters	79.3	19.7	1.0	9.7	42.3	48.0
Earth Day-Climate	74.9	24.5	0.6	9.7	42.4	48.0
WrestleMania	79.5	17.2	3.3	9.6	42.2	48.2
f^{gini}						
Mythos	63.5	35.5	1.0	5.7	37.0	57.3
Trump-Tariffs	60.8	38.0	1.2	5.8	37.0	57.3
The Masters	62.4	36.8	0.8	5.7	37.0	57.3
Earth Day-Climate	62.2	37.0	0.9	5.7	37.0	57.3
WrestleMania	65.4	32.2	2.4	5.7	36.9	57.3

Full three-tier breakdown across topics and f . Table 13 reports the complete three-tier shares ($R_{G_{\text{top}}}, R_{G_{\text{mid}}}, R_{G_{\text{tail}}}$) at the visibility-biased small panel ($N = 10^2$, mean over 10 seeds) and at the full panel, for all five topics under all four value functions of Section 3.1. The biased-vs-full gap on $R_{G_{\text{top}}}$ is positive in 20/20 cells; the gap on $R_{G_{\text{tail}}}$ is correspondingly negative. The magnitude varies systematically with the form of f : the linear baseline f^{lin} shifts $R_{G_{\text{top}}}^S$ by ≈ 20 pp, the saturating f^{heat} by 5 to 9 pp, and the concentration-flavored f^{var} and f^{gini} by 55 to 70 pp.

I Data ethics, privacy, and misuse considerations

User-level attribution on a real social platform raises legitimate concerns about privacy, the boundary of public data, de-identification of released artifacts, and the potential for misuse. We discuss each below.

Public-data boundary. Bluesky’s AT-Protocol exposes a Jetstream firehose [Failla and Rossetti, 2024, Seckin et al., 2025] that broadcasts every public event (post, reply, repost, follow) generated on the network. The firehose is public-by-design: a user posting on Bluesky is, by the platform’s own data model, opting into broadcast on this stream. Our pipeline reads only this public stream. We never access private direct messages, private accounts, draft content, locked accounts, age-verification metadata, IP addresses, or any signal that requires authenticated access. Bluesky requires age 18+ at signup, and bot-like accounts (handle heuristics, sub-7-day account-age cutoff, repetitive posting patterns) are filtered out before any analysis (Appendix H).

De-identification of released artifacts. Per-user identifiers (DIDs, handles, post URIs) are not released in any artifact. The open-source code accompanying this paper operates on opaque integer indices $i \in [N]$, with no map back to Bluesky identity in any released NPZ, CSV, or table. The mapping from index to DID exists only in our local pipeline and is never exposed in the released codebase or supplementary material. The pipeline scripts read the firehose live, so any reuse of the

codebase by a third party requires that party to re-fetch the public firehose under their own access; we do not redistribute Bluesky raw data.

Aggregation level. All numerical results reported in the paper, the appendix tables, and the released CSVs are aggregated to the panel, topic, value-function, sampling-strategy, follower-tier, follower-percentile-bin, or day level. We never report or release per-user attribution scores keyed to any identifier. The 100-bin follower-percentile aggregation (Figure 1(a)) is the finest granularity in any released artifact; even within a single bin, $|N|/100 \approx 16,716$ users contribute to each cell, well above any conventional k -anonymity threshold.

Misuse risk and mitigation. Our attribution method, applied at full scale, in principle allows a deployer who possesses identifier-keyed feature vectors to single out individual users by attribution magnitude. We do not enable this misuse: the released codebase emits attribution at the percentile-bin or follower-tier level only (the same aggregation used in the paper), and removing this aggregation requires non-trivial code modification by the user. Researchers extending our codebase to identifier-keyed attribution should follow the same convention and report only at aggregated levels. We also do not provide attribution at the individual-conversation, individual-thread, or individual-post level, so the codebase cannot be repurposed for content-level deanonymization.

Compliance. The data use complies with Bluesky’s Terms of Service for the public AT-Protocol firehose and with the AT-Protocol public-data conventions [Failla and Rossetti, 2024]. The work conforms to the NeurIPS Code of Ethics: it uses only public data aggregated across about 1.67 million users, applies no individual-level inference, releases no identifier-keyed user data, and does not require IRB review per the NeurIPS classification of human-subjects research (no enrollment, no intervention, no individual contact).

Scope of this appendix. The discussion above concerns the *empirical testbed* (Bluesky data, Section 3). For attribution applied to LLM-powered MAS simulations (Appendix P), the agents are synthetic and the same privacy concerns do not arise. However, if a future deployment uses our attribution on a hybrid system that includes human users (e.g. LLM-augmented social platforms), the same aggregation-level reporting recommendations apply.

J Reproducibility

The Bluesky firehose contents themselves cannot be redistributed: the AT-Protocol Terms of Service grant per-user public-broadcast access but do not authorize bulk redistribution by third parties. We instead make the analysis pipeline fully reproducible *from* the public firehose: given the specifications below and the code released as supplementary material, anyone with firehose access can recover the panel and the numbers reported in this paper deterministically.

Firehose endpoint and capture window. Data is captured live from the public Bluesky firehose during the window 2026-04-08T00:00:00Z to 2026-04-21T23:59:59Z (UTC). The capture script subscribes to the Jetstream WebSocket endpoint `wss://jetstream.atproto.com/subscribe` and writes one JSONL file per UTC day. Each line is a single event of one of four record types: `app.bsky.feed.post`, `app.bsky.feed.repost`, `app.bsky.feed.like`, or `app.bsky.graph.follow`. Anyone replaying the same Jetstream subscription against the same UTC window receives the same event stream up to the firehose’s eventual-consistency guarantees.

Filtering pipeline. Events are kept if (i) the actor’s account-age at window start is ≥ 7 days, (ii) the actor’s handle does not match a bot/automation regex (full table in the released code), and (iii) the actor produced at least one non-self-engagement event in the 14-day window. After all three filters the panel contains $|[N]| = 1,671,587$ users. The cleanup script is deterministic: rerunning on the same captured JSONL produces the same panel.

Topic matching. Each topic is defined by a small case-insensitive keyword/hashtag list applied over post text and hashtags. A post counts toward a topic if at least one keyword matches. The released code contains the exact keyword table per topic (Mythos, Trump-Tariffs, The Masters, Earth Day-Climate, WrestleMania).

Sampling seeds. Subset-sampling seeds are fixed to $\{0, 1, \dots, 9\}$ for the small-panel runs at $N \in \{10^2, 10^3, 10^4, 10^5\}$; the $N = 10^6$ and full-panel ($N = |[N]|$) runs are deterministic single-seed evaluations. Reported mean \pm std are computed over the ten seeds for the small-panel cells and

Table 14: Share gap $\Delta R_{G_k}(10^2 \rightarrow |[N]|) := R_{G_k}^{\text{bias},100} - R_{G_k}^{\text{full}}$ on Mythos with f^{heat} under three top-tier anchors: G_{top} (top 1% by followers), G_2 (top 1% by 7-day post count), and G_3 (top 1% by 7-day replies received). Mean over ten subset seeds.

Top-tier anchor	$R_{G_k}^{\text{bias},100}$	$R_{G_k}^{\text{full}}$	ΔR_{G_k} (pp)
G_{top} top-1% by followers	0.113	0.037	+7.6
G_2 top-1% by 7-day post count	0.241	0.140	+10.1
G_3 top-1% by 7-day replies received	0.213	0.121	+9.2

are absent (single value) for the full-panel cells. The visibility-pool selection (top 5% by composite visibility score; Appendix N) is itself a deterministic function of the panel.

Supplementary material. The supplementary archive contains: the firehose-capture script, the filtering and topic-matching pipeline, the attribution implementation for all four analytic value functions (f^{lin} , f^{heat} , f^{var} , f^{gini}), the experiment-orchestration scripts that reproduce every table and figure in the paper, and an end-to-end README.md. Running the full pipeline on a fresh firehose subscription requires the 14-day capture window in real time plus approximately 30 minutes of compute on a single CPU node for the attribution and aggregation steps. We will release the code under an open-source license at the camera-ready stage.

On the 2026 timestamps. The data is real and contemporaneous: it was captured in real time from the public Bluesky firehose during April 2026, the period of this paper’s preparation. The events discussed in Section 3.3 (the Masters Sunday final on April 13, 2026; WrestleMania night one on April 19, 2026; the Earth Day approach on April 22, 2026) are public events whose occurrence and timing can be cross-checked against any independent record.

K Top-tier anchor robustness

The flip in Section 3.2 is reported using the top-tier group G_{top} defined as the top 1% by follower count ($|G_{\text{top}}| = 16,716$). This appendix repeats the small-biased-versus-full comparison under two alternative top-tier anchors: G_2 , the top 1% by 7-day post count, and G_3 , the top 1% by 7-day replies received. The three anchors share only a small overlap (Jaccard $|G_{\text{top}} \cap G_2|/16,716 = 7.7\%$ and $|G_{\text{top}} \cap G_3|/16,716 = 20.1\%$), so they are largely independent definitions of “elite”. Table 14 reports the share gap $\Delta R_{G_k}(10^2 \rightarrow |[N]|)$ under each anchor on Mythos with f^{heat} . All three anchors yield a positive gap exceeding 5 percentage points; the gap is largest under G_{top} , the anchor most directly correlated with the visibility score that defines the biased pool, and smaller but still substantial under G_2 and G_3 . The direction of the flip is unchanged across all three anchors. The full-panel shares for G_2 and G_3 (14.0% and 12.1% respectively) are themselves about 3× larger than the full-panel share for G_{top} (3.7%), so the activity-elite (G_2) and resonance-elite (G_3) groups already carry a non-trivial fraction of the total attribution at full scale.

L Per-topic per-day attribution dynamics and 14-day stability

This appendix expands on the per-topic per-day structure visible in main-text Figure 1(a) and reports the 14-day stability of the small-biased flip. The peak-day decomposition for each topic under f^{heat} is summarised in Table 15: the sports peak on April 13 coincides with the Sunday final round of The Masters, the entertainment peak on April 19 with WrestleMania night one, and the society peak on April 16 falls in the run-up to Earth Day on April 22. The political and technology topics show flatter trajectories without a single dominant peak. The peak-day three-tier shares vary substantially across topics: WrestleMania’s peak is overwhelmingly tail-driven (82.1%), Earth Day’s peak has the largest G_{top} share (8.0%) of any topic-peak combination, and The Masters’s peak day shows the strongest mid-tier presence (24.7%).

The 14-day stability of the small-biased flip is summarised in Table 16, which reports the per-day G_{top} share $R_{G_{\text{top}}}^{(t)}$ on Mythos at six sample sizes under the visibility-biased protocol, aggregated to mean and standard deviation across the 14 days. The gap between $N = 10^2$ and $|[N]|$ remains in a narrow band across the entire window, so the flip is not driven by a few unusual days.

Table 15: Peak day per topic under f^{heat} at full scale, with the three-tier share ($R_{G_{\text{top}}}, R_{G_{\text{mid}}}, R_{G_{\text{tail}}}$) on that day and the corresponding real-world event.

Topic	Peak day	$R_{G_{\text{top}}}$	$R_{G_{\text{mid}}}$	$R_{G_{\text{tail}}}$	Real-world cue
Mythos	April 8	0.067	0.226	0.707	(no single event)
Trump-Tariffs	April 8	0.062	0.227	0.711	(no single event)
The Masters	April 13	0.044	0.247	0.709	Sunday final round
Earth Day-Climate	April 16	0.080	0.243	0.676	approach to April 22
WrestleMania	April 19	0.018	0.161	0.821	WrestleMania night one

Table 16: Per-day G_{top} share $R_{G_{\text{top}}}^{(t)}$ on Mythos under the visibility-biased protocol, $f = f^{\text{heat}}$, aggregated across the 14 days $t \in \{1, \dots, 14\}$ at six sample sizes. Each row reports the mean and standard deviation across the 14 daily values; for $N \leq 10^5$ the daily value is itself the mean over 5 subset seeds. Note that $R_{G_{\text{top}}}^{(t)}$ is computed per-day-then-averaged and therefore differs at small N from the 14-day-aggregate $R_{G_{\text{top}}}^S$ reported in Tables 2 and 18: the two coincide at the full panel but the per-day-then-averaged version is more concentrated at small N because per-day attribution variance does not commute with aggregation.

N	$R_{G_{\text{top}}}^{(t)}$ mean across 14 days	std across 14 days
10^2	0.452	0.034
10^3	0.293	0.021
10^4	0.165	0.011
10^5	0.084	0.006
10^6	0.042	0.003
$ \llbracket N \rrbracket $	0.037	0.002

M Macro attribution structure: by-bin, by-day breakdown

The full-scale attribution structure across all five topics, all 1,671,587 users, and all 14 days is shown directly in main-text Figure 1(a). For each topic, each day, and each follower-percentile bin we compute the within-bin attribution mass $M(t, p) := \sum_{i \in \text{bin } p} \phi_{i,t}^{[N]}$, with 100 equal-size percentile bins; the colour in Figure 1(a) is $\log_{10} |M(t, p)|$, the vertical axis is the follower-percentile bin (top: top 1%, bottom: lowest), and the horizontal axis is time. Two structural facts visible without any group concept: the top one or two rows are bright but thin, while the bottom 50–90 rows are pale individually but jointly sum to the larger contribution; and the time structure of each topic differs in a topic-specific way (sharp peaks for sports and entertainment, broader rises for politics and society, multi-peak patterns for the technology topic). The by-bin and by-day marginals (sums of $M(t, p)$ across days and bins respectively) reduce to Tables 15 and 16.

N Sampling strategies and dose-response

This appendix specifies the four sampling strategies used throughout the paper (one of which is the random control) and reports the dose-response between the G_{top} share of the small panel and the resulting flip magnitude. Each biased strategy encodes a research practice common in the LLM-powered MAS literature: visibility-weighted convenience sampling, topic-engagement-weighted convenience sampling, and topic-only convenience sampling. Together they cover the realistic range of how small- N studies in fact build their panels, with monotonically decreasing concentration of high-followers users in the resulting subset.

BIAS_{visibility}. Compute, for each user, a composite visibility score $v_i := z(\log(1 + \text{followers}_i)) + z(\log(1 + \text{topic_engagement}_i))$, where $z(\cdot)$ standardises to zero mean and unit variance over the full $|\llbracket N \rrbracket|$ panel and $\text{topic_engagement}_i = \text{topic_posts}_i + \text{topic_replies_received}_i$. Take the top 5% of users by v_i as a fixed visibility pool ($\approx 83,580$ users on Mythos), and draw N users uniformly at random from this pool. This is the default biased protocol of the main text.

Table 17: Average count of G_{top} agents in the sampled subset and the resulting flip magnitude $\Delta R_{G_{\text{top}}}$, by sampling protocol, on Mythos at $N = 10^2$ with f^{gini} , mean over ten subset seeds.

Strategy	Mean $ S \cap G_{\text{top}} $ (out of 100)	$\Delta R_{G_{\text{top}}}$ (pp, f^{gini})
BIAS _{visibility}	≈ 19.5	+57.8
BIAS _{topic_x_follow}	≈ 5.1	+12.8
BIAS _{topic_top}	≈ 1.5	+12.7
RAND	< 1	-1.2

BIAS_{topic_x_follow}. Sort users by the multiplicative score $(\log(1 + b_i + c_i)) \cdot \log(1 + \text{followers}_i)$, retain the top K as the pool with K matched to the topic’s active count ($\approx 5,000$ – $10,000$ depending on topic), and draw N uniformly from this pool. This protocol mirrors topic-focused case studies that filter to high-influence and topic-engaged users jointly.

BIAS_{topic_top}. Sort users by topic-engagement alone (b_i), retain the top K as the pool (matched to topic active count), and draw N uniformly. This protocol mirrors purely topic-focused studies that ignore generic visibility.

RAND. Draw N users uniformly at random from the full $[[N]]$ panel. This is the unbiased control.

For all four strategies, when $N \geq |\text{pool}|$, we take the full pool plus a random complement from $[[N]] \setminus \text{pool}$ to reach size N , which gracefully recovers $|S| = [[N]]$ at the full-panel limit. Subset seeds $\in \{0, 1, \dots, 9\}$ are independent.

Dose-response. Table 17 reports $\Delta R_{G_{\text{top}}}$ and the average $|S \cap G_{\text{top}}|$ for each of the four strategies on Mythos at $N = 10^2$, with f^{gini} chosen because it has the largest dynamic range of the four value functions. The dose-response is directionally monotone: **BIAS**_{visibility} pre-concentrates the most G_{top} agents into S (mean $|S \cap G_{\text{top}}| \approx 19.5$ out of 100) and produces by far the largest flip ($\Delta R_{G_{\text{top}}} \approx +57.8$ pp); the two milder biased protocols, **BIAS**_{topic_x_follow} and **BIAS**_{topic_top}, pre-concentrate substantially fewer G_{top} agents (≈ 5.1 and ≈ 1.5 respectively) and produce intermediate flips of similar magnitude ($\approx +12.8$ and $\approx +12.7$); **RAND** captures essentially no G_{top} agents (< 1) and produces no flip (≈ -1.2 , statistically indistinguishable from zero). The same pattern holds on the other three value functions, with magnitudes scaling as in Table 2; full numerics across the $4 \times 4 \times 5$ cell grid are in the released supplementary CSV.

Visibility-pool variant. Replacing the composite v_i in **BIAS**_{visibility} with a follower-only score $\log(1 + \text{followers}_i)$ on Mythos at $N = 10^2$ leaves the direction and order-of-magnitude of the flip unchanged across all four value functions ($\Delta R_{G_{\text{top}}}$ within 30% of the composite-pool numbers reported in Table 2); detailed numbers are in the released CSV. The flip is therefore not an artefact of the specific composite scoring used to define the visibility pool.

O Full Mythos cross-scale numerical tables

This appendix tabulates the cross-scale numerics on Mythos under f^{heat} for the visibility-biased and random sampling protocols across six sample sizes $N \in \{10^2, 10^3, 10^4, 10^5, 10^6, [[N]]\}$ (Table 18). All entries are means over ten subset seeds. Under the visibility-biased protocol, $R_{G_{\text{top}}}$ peaks near $N = 10^3$ rather than at $N = 10^2$ (because a one-hundred-user pool is dominated by mid-tier users that happen to dominate the visibility-pool composition), then decays smoothly toward the full-panel value as N grows past the visibility pool’s size of $\approx 83,580$ at which point the biased protocol can no longer sustain a concentrated $|S \cap G_{\text{top}}|$. Under the random protocol, $R_{G_{\text{top}}}$ stays close to the population fraction of 1% throughout, with extra variance at small N from the chance of catching a single high-attribution agent in G_{top} .

P LLM-powered MAS validation

This appendix validates the attribution method directly on three LLM-powered MAS scenarios, complementing the Bluesky stress test of Section 3. Each scenario inherits the original system’s macro indicator, modified only to be C^2 where the original used non-smooth components (e.g.

Table 18: Three-tier shares ($R_{G_{\text{top}}}, R_{G_{\text{mid}}}, R_{G_{\text{tail}}}$) on Mythos with f^{heat} as a function of sample size N , under visibility-biased and random sampling, with the full panel as the bottom row. Mean over ten subset seeds.

N	Visibility-biased			Random		
	$R_{G_{\text{top}}}$	$R_{G_{\text{mid}}}$	$R_{G_{\text{tail}}}$	$R_{G_{\text{top}}}$	$R_{G_{\text{mid}}}$	$R_{G_{\text{tail}}}$
10^2	0.113	0.367	0.520	0.008	0.097	0.895
10^3	0.124	0.501	0.375	0.009	0.094	0.897
10^4	0.107	0.473	0.420	0.011	0.091	0.898
10^5	0.097	0.439	0.464	0.018	0.092	0.890
10^6	0.060	0.296	0.644	0.030	0.155	0.815
$[[N]]$	0.037	0.199	0.764	0.037	0.199	0.764

max, indicators) by replacing them with their standard smooth surrogates (softmax, sigmoid). The surrogates are chosen to preserve the qualitative shape of the original indicator; we do not claim that conclusions about the smoothed indicator transfer mechanically to the original non-smooth simulator metric, and a quantitative gap analysis between the smoothed and original indicators on each scenario is left as a robustness check for future work. Table 19 summarises the headline results: our Aumann–Shapley attribution matches sampled Shapley wherever sampled Shapley remains feasible, and remains usable on MidScale-Social where sampled Shapley does not.

EconAgent [Li et al., 2024]. The original simulator captures macroeconomic activity with $N = 10$ household agents over $T \geq 30$ steps. Per-agent features used here: consumption, income, endogenous consumption rate, endogenous investment rate, endogenous labor, endogenous saving rate, and wealth. The macro indicator is a smooth (C^2) wealth-amplified macro-pressure risk that aggregates excess demand, budget stress, concentration, systemic gap, and instability into a single scalar. The baseline action zeroes out work, consumption, and investment for the target step while preserving wealth.

SocialLLM, a social propagation simulator with $N = 20$ agents in the spirit of Stauffer and Meyer-Ortmanns [2004]’s consensus model on a Barabási–Albert network. Per-agent features: belief, posted, views/interactions, likes, dislikes. The macro indicator is a smooth risky-expression risk. The baseline action puts the agent into a neutral non-posting state for the target step.

MidScale-Social. A lightweight large-scale propagation scenario with $N = 1000$ agents over $T = 30$ steps and 10 runs. A small set of LLM-generated personas, stances, and message prototypes seeds an otherwise deterministic propagation process. Features: belief or sentiment, exposure count, posting intensity, reshare intensity, and an influence-weight context. The macro indicator is a smooth influence-weighted propagation risk. This scenario is the only one of the three where sampled Shapley with 1,000 permutation samples becomes infeasible at evaluation time.

Faithfulness metric. For each scenario, we identify the target time t^* as the post-midpoint risk peak, $t^* = \arg \max_{t \geq \lceil T/2 \rceil} f(z_t)$. We then rank agents by attribution magnitude and report the deletion AUC obtained by replacing the top- k attributed agents with the baseline action and measuring the macro indicator’s drop, averaged over $k = 1, \dots, K$.

Reading the table. On EconAgent, our attribution and sampled Shapley agree to Kendall $\tau = 0.80$ with full top-10 overlap, and the deletion AUC matches to within 0.01 (0.516 vs 0.524); both substantially exceed the random baseline (0.174). On SocialLLM the deletion test saturates: the macro indicator after top- k replacement is largely insensitive to which k agents are removed once k is small, so all three axiomatic methods land on the same AUC. We report this transparently as a property of the scenario rather than of the methods, and rely on the rank-agreement metrics ($\tau = 0.96$, $J_{10} = 0.98$ against sampled Shapley) to distinguish them on SocialLLM. On MidScale-Social, sampled Shapley with 1,000 permutation samples is impractical at our compute budget: each run requires $1,000 \times 1,000$ value evaluations with the macro indicator costing $\Omega(N)$ per evaluation, so a single run sits at $\sim 10^9$ macro-indicator operations (multiple minutes per seed in our Python implementation), which puts the multi-seed sweep across the 10 runs out of reach for the experiment timeline. Our attribution and LOO produce identical small AUC values (0.008), one order of magnitude above the random baseline (0.001).

Table 19: Deletion-faithfulness metrics across three LLM-powered MAS scenarios. “Ours” is the Aumann–Shapley attribution of Appendix F. “ τ vs. Shapley” and “ J_{10} vs. Shapley” are Kendall τ and top-10 Jaccard against sampled Shapley as the agent-ranking reference; “= ref” marks the reference row itself, and “–” marks cells where sampled Shapley is infeasible at $N = 10^3$ (MidScale-Social).

Scenario	Method	Deletion AUC	Drop@5 (%)	τ vs. Shapley	J_{10} vs. Shapley
EconAgent	Ours	0.516	75.7	0.80	1.00
	Sampled Shapley	0.524	77.1	= ref	= ref
	LOO	0.517	76.1	0.80	1.00
	Random	0.174	40.0	–	–
SocialLLM	Ours	0.153	32.3	0.96	0.98
	Sampled Shapley	0.153	32.3	= ref	= ref
	LOO	0.153	32.3	0.95	0.91
	Random	0.100	21.2	–	–
MidScale-Social	Ours	0.008	1.5	–	–
	LOO	0.008	1.5	–	–
	Random	0.001	0.2	–	–

Table 20: Ranking agreement between attribution under the linear path $\tau \mapsto \tau_{z_S}$ and under a random-permutation piecewise-linear path, on SocialLLM and MidScale-Social. Kendall τ (mean and minimum) and top-10 overlap.

Scenario	Kendall τ (mean)	Kendall τ (min)	Top-10 overlap
SocialLLM	0.951	0.874	9.9/10
MidScale-Social	0.99999	0.99998	10.0/10

Bottom line. Wherever an axiomatic baseline (sampled Shapley) is feasible, our attribution agrees with it on agent rankings ($\tau \geq 0.80$, top-10 overlap $\geq 9.8/10$); where it is not feasible, ours remains computable. The Bluesky stress test of Section 3 is therefore not the only LLM-powered MAS evidence in the paper: the same attribution method ranks agents consistently with the gold-standard reference in two scenarios where the reference can be evaluated, and is the only feasible axiomatic option at $N = 10^3$.

Q Robustness sweeps

This appendix consolidates three robustness sweeps. Integration-step convergence (K) is reported in Appendix C (Table 5); baseline choice is reported in Appendix E (Table 10); path choice is reported here, plus an f -sensitivity sweep on MidScale-Social.

Path-choice ablation. The default linear path between z^0 and z_t can be replaced by a piecewise-linear path that fades each agent’s features in following a random permutation of the agent index (a coordinate-by-coordinate path). On SocialLLM and MidScale-Social, we measure (i) the Kendall τ between the resulting attribution rankings and (ii) the size of the top-10 overlap. The two paths agree to a Kendall τ above 0.95 on SocialLLM and above 0.99999 on MidScale-Social, with top-10 overlap 9.9/10 and 10/10 respectively (Table 20).

f -sensitivity ablation on MidScale-Social. We test three plausible value functions: f_1 a weighted-sum aggregator, f_2 a log-aggregate ($\log(1 + \sum)$), and f_3 an interaction aggregator with explicit pairwise terms. Pairwise comparisons (Table 21) yield top-10 overlap above 9/10 in every case; weighted sum and log aggregator are nearly indistinguishable (Kendall $\tau \geq 0.984$).

Topic and strategy consistency. The cross-scale flip persists across all five Bluesky topics and all four analytic value functions (main-text Table 2 and Table 13, 20/20 cells positive), and across all three biased sampling protocols ($\text{BIAS}_{\text{visibility}}$, $\text{BIAS}_{\text{topic_x_follow}}$, $\text{BIAS}_{\text{topic_top}}$ in Appendix N); the random control RAND produces no flip on any topic or value function. The top-10 Jaccard recovery $J_{10}(N, |[N]|)$ in Table 12 confirms that the small panel also fails to recover the identity of the top-10 agents on every topic.

Table 21: Pairwise ranking agreement between attribution under three plausible value functions on MidScale-Social: f_1 (weighted-sum aggregator), f_2 (log-aggregate), and f_3 (interaction aggregator with pairwise terms). Kendall τ and top-10 overlap.

Pair	Kendall τ (mean)	Kendall τ (min)	Top-10 overlap
f_1 vs. f_2	0.985	0.984	9.6/10
f_1 vs. f_3	0.909	0.905	9.2/10
f_2 vs. f_3	0.902	0.897	9.0/10

R Scaling-laws context

The N -dependence we report is orthogonal to the parameter-count scaling laws for language models [Kaplan et al., 2020, Hoffmann et al., 2022]; our N counts *agents* acting in the simulated multi-agent system, not parameters of the language model that powers each agent. Holding the per-agent LLM and prompt fixed, increasing N alters the interaction graph and the cross-agent contribution structure, which is what drives the attribution flip in Theorem 1(ii) and Section 3. Conversely, language-model scaling laws operate at the sub-agent level and do not predict the macroscopic flip studied here. The two notions of scale are complementary rather than substitutable.

S Further limitations and scope caveats

This appendix consolidates two scope caveats beyond the main-text caveat in Section 5.

Feature standardisation. We do not standardise the per-agent Reach–Activity–Resonance features beyond their natural log scale (Appendix H). The raw log scale is what controls how the four value functions weight different agents, and standardisation interacts non-trivially with f^{heat} ’s multiplicative-saturating form: z -scoring shifts the per-coordinate means m_a, m_b, m_c to zero and changes the position of the $\log(1 + H)$ saturation, which in turn changes the per-agent attribution magnitudes in a non-uniform way. We therefore report on the raw log scale throughout and leave a full standardisation sweep as a robustness check for future work.

LLM-driven macro indicators at million-agent scale. Our LLM-driven validation in Appendix P tops out at $N = 10^3$ (MidScale-Social); the million-agent evidence comes from analytic value functions on Bluesky (Section 3). The combination “LLM-driven macro indicator at $N = 10^6$ ” is therefore not directly tested in this paper. The path-integral attribution itself is agnostic to whether f is analytic or LLM-driven (Equation 3 requires only C^2 regularity), and the wall-clock numbers in Table 9 suggest the bottleneck at $N = 10^6$ would be one autograd backward pass through the LLM-driven f , which is hardware-dependent. Direct empirical validation at this combined scale is the natural next step.